Cell Reports

Article

Chemogenetic tuning reveals optimal MAPK signaling for cell-fate programming

Graphical abstract

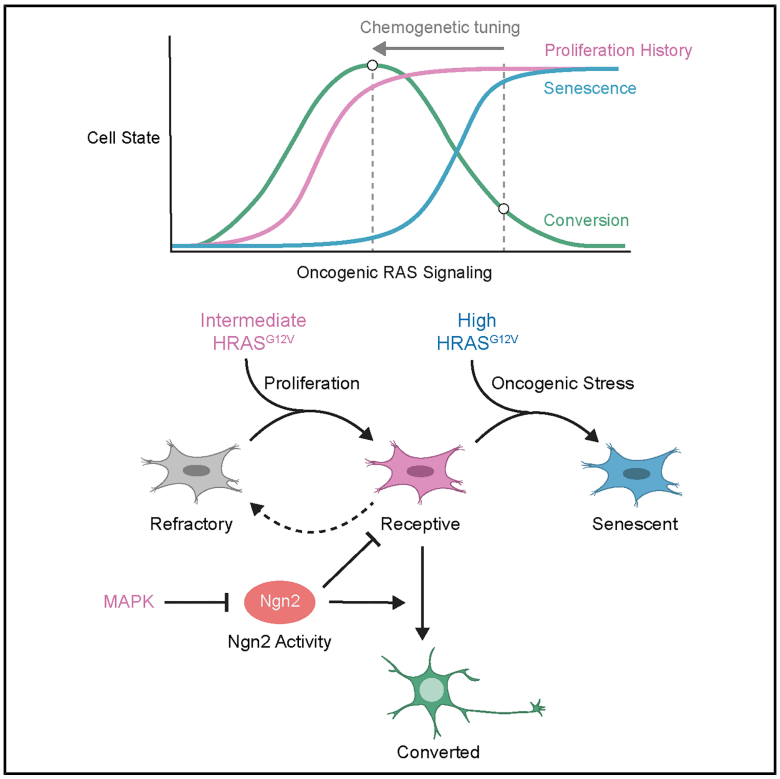

Highlights

- MAPK signaling drives proliferation and conversion of fibroblasts to motor neurons
- Cell-fate programming responds biphasically to *HRAS*^{G12V} expression
- A small-molecule MAPK inducer can replace *HRAS*^{G12V} for high rates of conversion
- MAPK signaling alters Ngn2 levels, influencing proliferation and conversion

Authors

Brittany A. Lende-Dorn, Jane C. Atkinson, Yunbeen Bae, Kate E. Galloway

Correspondence

katiegal@mit.edu

In brief

Using a well-defined model of direct conversion, Lende-Dorn et al. demonstrate that an optimal "Goldilocks" level of MAPK signaling efficiently drives cell-fate programming. Chemogenetic tuning of MAPK activity balances proliferation and transcription factor levels to support high rates of conversion to motor neurons.

Lende-Dorn et al., 2025, Cell Reports *44*, 116226
September 23, 2025
https://doi.org/10.1016/j.celrep.2025.116226

CellPress

Cell Reports

CellPress
OPEN ACCESS

Article

Chemogenetic tuning reveals optimal MAPK signaling for cell-fate programming

Brittany A. Lende-Dorn,[1] Jane C. Atkinson,[1] Yunbeen Bae,[1] and Kate E. Galloway[1,2,*]
[1]Department of Chemical Engineering, MIT, Cambridge, MA 02139, USA
[2]Lead contact
*Correspondence: katiegal@mit.edu
https://doi.org/10.1016/j.celrep.2025.116226

SUMMARY

Cell states evolve through the combined activity of signaling pathways and gene networks. While transcription factors can direct cell fate, these factors rely on a receptive cell state. How signaling levels contribute to the emergence of receptive cell states remains poorly defined. Using a well-defined model of direct conversion, we examined how levels of the mitogen-activated protein kinase (MAPK)-activating oncogene *HRAS*^{G12V} influence direct conversion of primary fibroblasts to induced motor neurons. The rates of direct conversion respond biphasically to increasing *HRAS*^{G12V} levels. An optimal "Goldilocks" level of MAPK signaling efficiently drives cell-fate programming, whereas high levels of *HRAS*^{G12V} induce senescence. Through chemogenetic tuning, we set the optimal MAPK activity for high rates of conversion in the absence of *HRAS* mutants. In addition to proliferation, MAPK signaling influences conversion by regulating Ngn2 activity. Our results highlight the need to tune therapeutic interventions within a non-monotonic landscape that is shaped by genetics and levels of gene expression.

INTRODUCTION

The activity of the mitogen-activated protein kinase (MAPK) pathway translates extracellular cues into changes in gene regulatory networks to shape cell-fate decisions.[1–6] Pathway activity regulates critical cellular functions such as proliferation, differentiation, and survival. In the canonical MAPK cascade, the upstream RAS GTPase signals to RAF. Phosphorylation of RAF relays through the MAPK cascade from MEK to ERK, which translocates to the nucleus to regulate gene activity (Figure 1A). Nearly half of all tumors include activating mutations in receptor tyrosine kinases, *RAS*, or other MAPK pathway species.[7] Among these MAPK mutations, *RAS* mutation is the most frequent, appearing in nearly a quarter of cancers.[8] Mutations that lock *RAS* in its active GTP-bound state persistently stimulate downstream pathways to drive tumorigenesis.[9] The strength and dynamics of MAPK signaling influence cell fate.[1,6] Strong aberrant signaling triggers pathways that drive cells to terminal fates, whereas intermediate levels of signaling support proliferation and self-renewal.[10–13]

While MAPK signaling contributes to diverse processes to support cell-fate transitions, understanding how these pathways direct changes in cell identity remains challenging. Combinations of genetics and the dynamics of gene expression contribute to cell-fate outcomes.[4,14–17] Dynamic and non-monotonic relationships can obscure the inference of causal relationships between profiles of gene expression and cell fates.[18–20] In cellular reprogramming, the addition of *c-MYC*, a downstream target of the MAPK pathway, increases the rates of reprogramming to induced pluripotent stem cells (iPSCs).[21–23] However, mild inhibition of MEK increases the total number of reprogrammed cells.[24] In differentiation of embryonic stem cells (ESCs), attenuation of ERK signaling via MEK inhibition prohibits differentiation into neural lineages,[25,26] whereas the inhibition or knockdown of *RSK1*, a negative regulator of MAPK signaling, accelerates ESC differentiation.[27] However, complete knockout of signaling nodes such as *RAS* and *ERK1/2* in mouse ESCs results in growth arrest, limited differentiation, and apoptosis.[28,29] *In vivo* and *in vitro*, the dynamics of MAPK signaling can dictate whether cells differentiate, die, or continue to divide.[1,6] Notably, modulating ERK activity can rewire cell fates.[1] Depending on the context, MAPK signaling can either increase or decrease the rates of specific cell-fate transitions, suggesting the complex processing of these dynamic signals.

Understanding the functional relationship between MAPK signaling and cell-fate transitions presents several challenges. Intrinsic and extrinsic variation can generate subpopulations that respond differently to cell-fate cues, obscuring connections between cell states and resulting cell fates.[19,30–34] Even in genetically homogenous populations, the asynchronous and stochastic nature of cell-fate transitions makes observing and quantifying these events challenging.[35–37] Consequently, many phenotypes that contribute to cell-fate transitions are studied in immortalized cell lines and stem cells, where genetic tools can be uniformly installed to map cell state to cell fate.[19,20,38–40] However, the underlying genetic background for immortalization may limit the translatability of the findings from these systems to primary cells.

To investigate how healthy primary cells transition between somatic identities, we have recently developed a system of

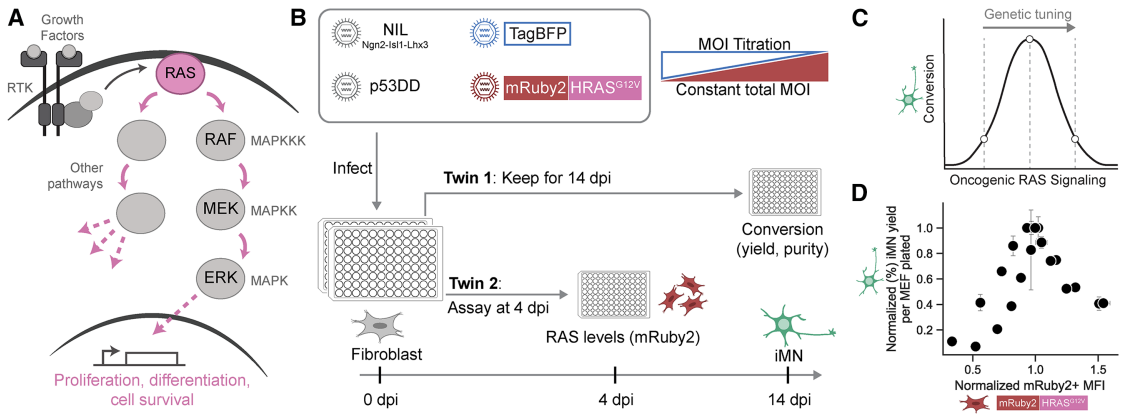

Figure 1. Cell-fate programming responds biphasically to titration of *HRAS^{G12V}*

(A) Simplified diagram of RAS signaling, with a focus on the mitogen-activated protein kinase (MAPK) pathway consisting of RAF, MEK, and ERK downstream of *RAS*.

(B) Schematic depicting viral delivery strategy of conversion cocktail. NIL (Ngn2, Isl1, and Lhx3 neuronal transcription factors) and *p53DD* (a *p53* mutant) are delivered on retrovirus. mRuby2-tagged *HRAS^{G12V}* is delivered on lentivirus with expression driven by a CAG promoter. A "filler" lentivirus expressing TagBFP is included to keep the lentiviral multiplicity of infection (MOI) constant for varying mRuby2-*HRAS^{G12V}* amounts. In a twin assay, two identical plates of cells are infected with the conversion cocktail. At 4 days post-infection (dpi), mRuby2-*HRAS^{G12V}* expression levels are measured, and at 14 dpi, the iMN yield and purity are quantified.

(C) Diagram depicting expected conversion results with mRuby2-*HRAS^{G12V}* MOI titration.

(D) Normalized iMN yield at 14 dpi vs. mRuby2-*RAS*+ geometric mean fluorescent intensity (MFI) at 4 dpi. Each point represents the mean of $n = 3$ technical replicates per bioreplicate ± standard error of mean (SEM). iMN yield is normalized so the maximum yield for each replicate overlays at 1.0 on the *y* axis, and the mRuby2 levels are normalized so the mRuby2+ MFI at the MOI corresponding to the peak iMN yields overlays at 1.0 on the *x* axis. $n = 4$ biological reps per condition.

direct conversion that generates induced motor neurons (iMNs) at high rates.[30–33] To improve our ability to track states that result in successful conversion, we have recently improved the robustness and efficiency of conversion to generate larger numbers of converted cells.[30–32] High rates of conversion offer the statistical power to draw inferences between cell states and cell fates in response to chemical and genetic perturbations.[30–32,41,42] Further, we can accurately estimate the number of conversion events based simply on the number of neurons generated, which is not possible in transitions to mitotic cells. As post-mitotic cells, neurons do not divide. Thus, each neuron corresponds to exactly one conversion event. This direct conversion system provides a unique platform to systematically investigate the role of MAPK signaling across distinct stages of cell-fate transitions.

Inclusion of *HRAS^{G12V}* substantially increases the rates of conversion of mouse embryonic fibroblasts.[30–32] However, the specific impact of the levels of *HRAS^{G12V}* expression and the influence of MAPK signaling on direct conversion have not been previously defined. In this study, we systematically varied *HRAS^{G12V}* levels, explored the stoichiometric effects of multigene cassettes, and tested small-molecule regulators of the MAPK pathway to dissect their contributions to cell-fate programming. Our findings reveal a biphasic relationship between oncogenic *RAS* levels and conversion rates, demonstrating that high MAPK activity drives senescence, while moderate MAPK activity promotes proliferation and optimizes yield. By replacing *HRAS^{G12V}* with a small-molecule inducer of MAPK signaling, we maintained high rates of conversion while eliminating oncogenic *RAS*. We also demonstrate that disrupting Ngn2 phosphorylation impairs proliferation and thus conversion yield, supporting a model in which MAPK signaling regulates Ngn2 activity to balance both the proliferation and induction of a post-mitotic, neuronal cell fate. Overall, our results advance our understanding of the role of oncogenic *RAS* and MAPK signaling in our high-efficiency direct conversion, offering insights for downstream translational applications.

RESULTS

Cell-fate programming responds biphasically to the titration of *HRAS^{G12V}*

Oncogenes drive proliferation and cell-fate programming (Figure 1A).[35,36,43–45] To examine how the expression levels of MAPK mutants affect cell-fate transitions, we used a well-defined model of direct conversion.[30–33,42] In this model system, the transduction of mouse embryonic fibroblasts with a single cassette of transcription factors (*Ngn2*, *Isl1*, and *Lhx3* [NIL]) drives their conversion to motor neurons (Figure 1B).[31,32] We can monitor conversion and quantify conversion events based on the activation of the motor neuron reporter, *Hb9*::*GFP*, from transgenic mouse embryonic fibroblasts. Unlike other cell-fate transitions, such as oncogenic transformation or conversion to mitotic cell types, direct conversion to a post-mitotic identity allows us to accurately quantify the number of conversion events based simply on the number of neurons.[30–32]

The introduction of transcription factors alone induces low rates of conversion (Figures S1A–S1D). Expanding the population of hyperproliferative (HyperP) cells by introducing mutant *p53* (*p53DD*, a *p53* mutant that lacks the DNA-binding domain), mutant *RAS* (*HRAS^{G12V}*), and a small-molecule transforming

CellPress
OPEN ACCESS

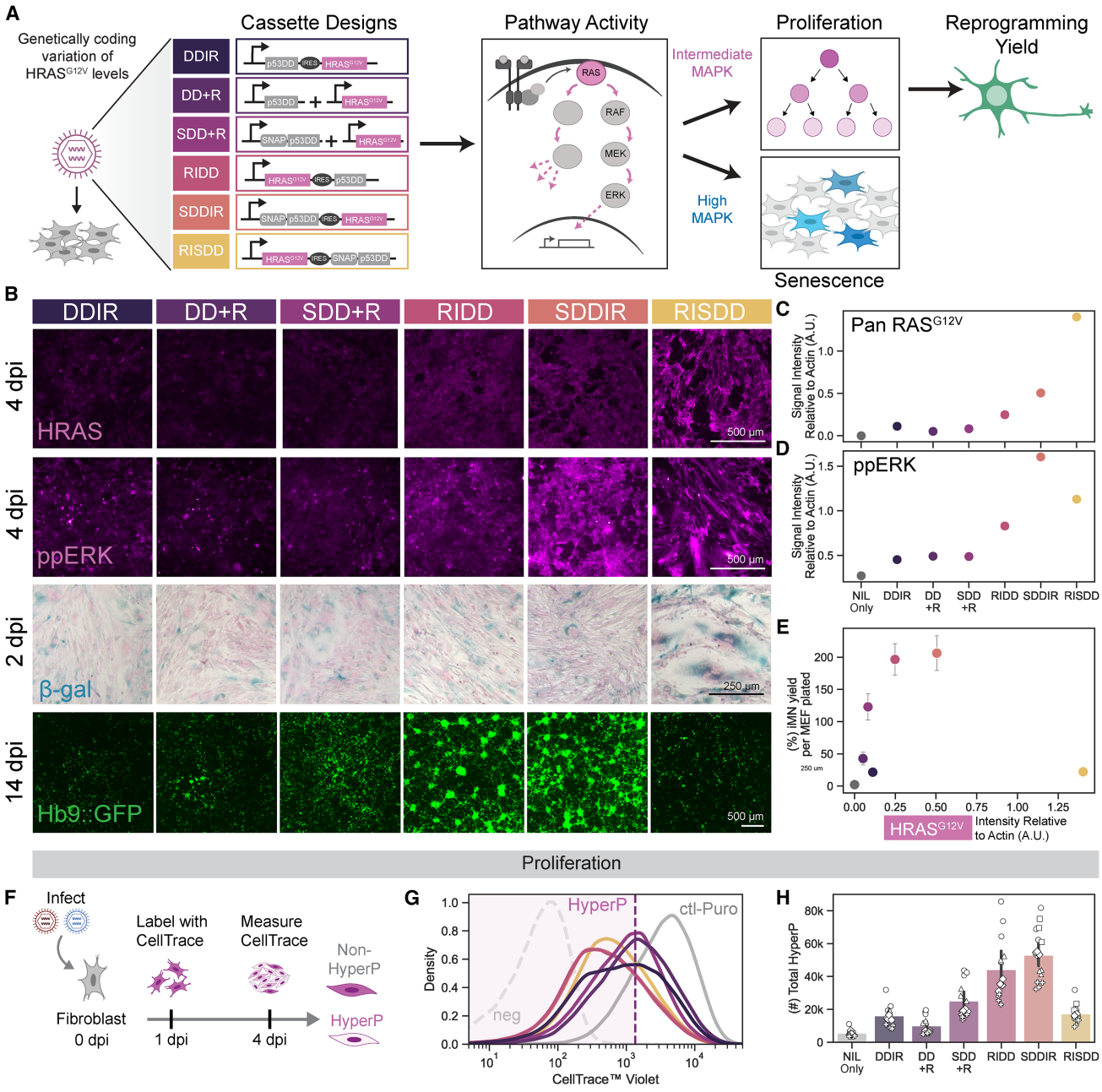

Figure 2. *HRAS*^{G12V} produces biphasic conversion through MAPK signaling and proliferation

(A) Schematic depicting polycistronic cassette designs expressing *HRAS*^{G12V} and either *p53DD* or SNAP-*p53DD*, separated by an internal ribosomal entry site (IRES). Transduced cells were analyzed for phenotypes that are expected to change with varying RAS expression levels. Conversion conditions always include NIL transcription factors.

(B) Representative images of immunofluorescent staining for *HRAS* and ppERK at 4 days post-infection (dpi), cells stained for senescence-associated β--galactosidase (β-gal) and nuclear fast red at 2 dpi, and *Hb9::GFP* expression in iMNs at 14 dpi. Scale bars represent 500 μm for *HRAS*, ppERK, and *Hb9::GFP* images and 250 μm for β-gal images.

(C) Pan-*RAS*^{G12V} expression levels quantified from a western blot and normalized to β-actin levels.

(D) ppERK levels quantified from a western blot and normalized to β-actin levels.

(E) iMN yield at 14 dpi vs. Pan-*RAS*^{G12V} expression normalized to β-actin levels measured from a western blot. iMN yield is shown as mean ± standard error of mean (SEM).

(F) Diagram depicting cell proliferation assay. Cells are labeled with CellTrace dye at 1 dpi, and fluorescent signal is measured at 4 dpi. Cells with a lower CellTrace signal have proliferated more than cells with a higher signal.

(legend continued on next page)

growth factor β (TGF-β) inhibitor (RepSox) dramatically increases the conversion yield.[30–32] As expected, transcriptional profiling shows that the addition of *p53DD* broadly increases the expression of proliferation markers and reduces the activation of *p53* gene targets (Figures S1E–S1J). In particular, reduction in *p21* transcripts, a direct target of p53 transcriptional regulation and a cell cycle inhibitor, may link these p53-mediated processes (Figure S1I). This transient HyperP population is highly receptive to transcription factors, converting at four times the rates of other cells in the same conditions.[31,33] By driving proliferation, the levels of the mutant *HRAS* may influence the abundance and fate of this receptive population. To measure the levels of $HRAS^{G12V}$, we added an N-terminal mRuby2 tag with a flexible GSG linker. To directly investigate how *RAS* expression levels affect conversion, we titrated the multiplicity of infection (MOI) of a lentivirus encoding *mRuby2-HRAS*^{G12V} (Figures 1B and S2A–S2H). To ensure that conversion changes were not influenced by variations in the total viral burden, we included a second lentivirus expressing TagBFP to maintain a constant viral load (i.e., total MOI) across conditions (Figure 1B). As expected, the level of mRuby2-$HRAS^{G12V}$ increases with MOI (Figure S2C).

Previous work indicates that the proliferation of epithelial cells increases non-monotonically in response to MAPK signaling.[4] Thus, we hypothesized that conversion would respond non-monotonically to increasing levels of mRuby2-$HRAS^{G12V}$ (Figure 1C). To define how levels of $HRAS^{G12V}$ affect cell-fate programming, we used a twin-plate assay to map the expression levels of $HRAS^{G12V}$ to conversion events. In a twin-plate assay, we measure mRuby2-$HRAS^{G12V}$ levels at 4 days post-infection (dpi) from one plate of cells and measure conversion via *Hb9*::*GFP* activation at 14 dpi from a second "twin" plate (Figure 1B).

Rapidly proliferating cells are smaller and show lower levels of transgene expression.[31,33] To control for proliferation-mediated differences, we normalized the mRuby2 fluorescence intensities and conversion yields across conditions and replicates (Figures S2D–S2H). Normalizing by replicate allows us to control for the combined batch effects of virus and primary mouse embryonic fibroblasts. We normalized each replicate to the MOI corresponding to the peak iMN yield within that replicate. This normalization reveals a clear biphasic correlation between mRuby2-$HRAS^{G12V}$ levels and conversion yield (Figure 1D). These results indicate that optimal conversion rates are driven by intermediate levels of RAS expression. Additionally, we examined the effect of mRuby2-$HRAS^{G12V}$ levels on conversion with a SNAP-tagged *p53DD* that allows us to visualize *p53DD* expression in the presence of a fluorescently labeled SNAP substrate. While both variants show a biphasic conversion response, SNAP-*DD* increases the total yield of neurons and reduces the absolute optimal levels of mRuby2-$HRAS^{G12V}$ (Figures S1A–S1D). Thus, the exact optimal level of RAS expression depends on the properties of the *p53* mutant (Figures 1D, S1D, S2E, and S2F). Together, our data indicate that an optimal level of $HRAS^{G12V}$ drives cell-fate transitions. The identity and properties of genetic variants can tune the optimum $HRAS^{G12V}$ level and the rates of conversion.

$HRAS^{G12V}$ produces biphasic conversion through MAPK signaling and proliferation

Overexpression of $HRAS^{G12V}$ drives MAPK signaling.[8,46] Thus, we hypothesized that increasing $HRAS^{G12V}$ expression levels increase the rates of proliferation and conversion by inducing MAPK signaling (Figure 2A). To limit extrinsic variation associated with different copy numbers, we encoded both $HRAS^{G12V}$ and *p53* mutants on a single viral transcript upstream and downstream of an internal ribosomal entry site (IRES). The relative ordering of genes around an IRES can generate different ratios of transgene expression while controlling for relative copy number.[47] Therefore, we expected to observe a range of $HRAS^{G12V}$ levels and conversions rates across cassettes with minimal genetic sources of extrinsic variance.

We compared four different single-transcript designs to the dual-virus delivery conditions (Figure 2A). To measure $HRAS^{G12V}$ expression levels across all conditions, we used immunofluorescent staining (Figure 2B) and western blot quantification (Figures 2C and S3A–S3E). At 4 dpi, we observed a wide range of $HRAS^{G12V}$ levels across conditions. By western blot, the overexpression of $HRAS^{G12V}$ ranges from 2 to 20 times the endogenous pan-RAS levels (Figures S3A and S3C). When we order conditions by levels of $HRAS^{G12V}$ expression, we find a biphasic relationship between $HRAS^{G12V}$ levels and conversion (Figures 2B, S3F, and S3G). MAPK signaling increases the phosphorylation of the downstream MAP kinase, ERK1/2. To examine MAPK signaling activity across conditions, we measured the levels of phosphorylated ERK1/2 (ppERK). As expected, both western blot and immunofluorescence imaging indicate that the levels of ppERK correlate with those of $HRAS^{G12V}$ (Figures 2B and 2D). At the highest levels of $HRAS^{G12V}$, we observe substantial increases in β-actin staining, reducing the normalized signal of ppERK (Figures 2D and S3B). Increases in β-actin align with changes that we observe in cell size at high levels of $HRAS^{G12V}$ and reports of proteome remodeling in large cells.[48] Plotting the $HRAS^{G12V}$ levels—as quantified from a western blot—against the iMN yield at 14 dpi confirmed the biphasic response (Figures 2E and S3H), consistent with the results from the mRuby2-$HRAS^{G12V}$ MOI titration (Figure 1D). Together, these data indicate that optimal levels of $HRAS^{G12V}$ induce an optimal level of MAPK signaling for high rates of conversion.

Proliferation drives cells to a state that is highly receptive to lineage-specifying transcription factors.[30–33] As MAPK signaling induces cellular proliferation, we hypothesized that optimal levels of $HRAS^{G12V}$ expression support conversion by increasing the population of HyperP cells. To assess proliferation history across conditions, we performed a CellTrace dye dilution assay. Cells were labeled at 1 dpi, and CellTrace signal was analyzed at 4 dpi using flow cytometry (Figure 2F). Lower CellTrace signal indicates a history of more proliferation. We denote HyperP cells

(G) Representative histograms of CellTrace levels at 4 dpi across conditions. Hyperproliferative (HyperP) cells are gated at the 20% lowest CellTrace signal in a control Puro (ctl-Puro) infected condition for a given biological replicate.
(H) Total number of HyperP cells at 4 dpi across conditions. Mean is shown with 95% confidence interval; marker style denotes biological reps; $n = 4$ biological reps per condition.

as the 20% lowest CellTrace signal in the control condition (Figure 2G). As expected from the conversion rates, we observe that increasing $HRAS^{G12V}$ levels increase the total number of HyperP cells up to a point. Above this threshold, increasing $HRAS^{G12V}$ levels reduce the number of HyperP cells and the conversion rate (Figures 2E, 2H, and S3F–S3I). In particular, we found that the RAS-IRES-SNAP-p53DD (RISDD) condition, which had the highest $HRAS^{G12V}$ and elevated MAPK signaling levels, consistently produces lower rates of conversion.

In diverse primary cells, the overexpression of mutant *HRAS* leads to oncogene-induced senescence.[49–57] Senescence is a state of permanent cell-cycle arrest associated with metabolic changes.[58] Staining for β-galactosidase (β-gal), a senescence marker, reveals an increase in cells with a strong β-gal signal in the RISDD condition (Figure 2B). Morphologically, we observed that cells with a strong β-gal signal are very large and flat (Figure S3J), another signature of senescence.[59]

Although the RISDD condition had fewer HyperP cells, the fraction of HyperP cells was unexpectedly high, despite the low overall cell numbers (Figure S3I). Potentially, cell death may contribute to a loss of total cell number. Transcriptome profiling of viable cells at 4 dpi showed reduced expression of proliferation markers in conditions with RISDD compared with SNAP-p53DD-IRES-RAS (SDDIR) (Figure S3L). However, RISDD also exhibited broadly elevated expression of apoptosis-related genes and senescence markers relative to SDDIR (Figures S3M and S3N). Notably, RISDD generates higher levels of *p21*, a key transcriptional target of *p53* and a widely used marker for senescence alongside β-gal staining (Figure S3N).[58,59] These findings suggest that while cells with RISDD can retain proliferative capacity, RISDD also increases the rates of cells undergoing apoptosis or growth arrest via senescence.

Oncogenic *RAS* can activate *p53* in response to oncogenic stress.[49–52,60] Western blots showed higher levels of *RAS* and lower levels of SNAP-*DD* in RISDD compared with SDDIR (Figures S3C and S3D). The ratio of SNAP-*DD* to $HRAS^{G12V}$ may influence the cells' response. We hypothesize that insufficient *p53DD* expression induces senescence in RISDD due to elevated oncogenic *RAS* signaling. These results further suggest that the optimal level of *RAS* signaling may depend on the degree of p53 inhibition provided by *p53DD*.

Our results demonstrate that low levels of $HRAS^{G12V}$ limit MAPK signaling, proliferation, and conversion. Conversely, excessive $HRAS^{G12V}$ expression elevates MAPK signaling to levels that induce senescence. This balance between proliferation and senescence creates a biphasic response of cell fate to $HRAS^{G12V}$ levels.

Tuning MAPK signaling attenuates senescence and increases conversion

Putatively, high levels of $HRAS^{G12V}$ drive oncogene-induced senescence through MAPK signaling. At the highest levels of oncogenic *RAS* expression, the inhibition of MAPK signaling could rescue conversion (Figure 3A). To test this hypothesis, we treated cells expressing high levels of $HRAS^{G12V}$ with PD0325901, an MEK inhibitor (MEKi), from 1 to 14 dpi. MEKi blocks MAPK signaling downstream of RAS by inhibiting MEK1/2-mediated transmission of signaling to ERK1/2.

We compared the effect of MEKi at two levels of $HRAS^{G12V}$ expression: intermediate and high. At high levels of $HRAS^{G12V}$ expression, we expect that MEKi will increase proliferation and conversion. From the model of conversion following a biphasic response, we expect that MEKi treatment at intermediate levels of $HRAS^{G12V}$ will reduce conversion (Figure 3A). In conversion, we used two polycistronic cassettes that code for identical proteins but generate intermediate and high levels of $HRAS^{G12V}$ expression—SDDIR and RISDD, respectively (Figures 3B–3D). We confirmed that MEKi reduces ppERK levels at 4 dpi in a dose-dependent manner (Figures 3D and S4A–S4D). At intermediate levels of $HRAS^{G12V}$ (i.e., the SDDIR condition), MEKi treatment reduces the number and fraction of HyperP cells at 4 dpi and the rate of conversion (Figures 3B–3D, S4E, and S4F). Conversely, at the highest levels of $HRAS^{G12V}$ (i.e., the RISDD condition), low concentrations of MEKi increase proliferation and conversion. Thus, MEKi treatment rescues conversion yield at high $HRAS^{G12V}$ expression, while MEKi reduces conversion yield at intermediate levels of $HRAS^{G12V}$ expression. Together, these data reinforce the idea that optimal levels of $HRAS^{G12V}$ expression drive conversion by tuning MAPK activity within an optimal regime.

Inhibiting MAPK activity at high levels of $HRAS^{G12V}$ expression may promote conversion by driving proliferation while limiting senescence. To investigate whether MEKi mitigates $HRAS^{G12V}$-induced senescence, we treated cells expressing high levels of $HRAS^{G12V}$ (i.e., RISDD condition) with varying MEKi concentrations at 1 dpi. We stained for senescence-associated β-gal at 2 dpi. MEKi reduces the number of cells showing a strong β-gal signal (Figure 3D). At 14 dpi, iMNs do not show strong β-gal signals (Figure S4G), indicating that β-gal staining is unrelated to the iMN state.

Recognizing that *RAS* activates other signaling pathways, we tested whether inhibiting the phosphoinositide 3-kinase (PI3K) or c-Jun N-terminal kinase (JNK) pathways affects the rate of conversion in the RISDD condition. Immunofluorescent staining for phospho-AKT (pAKT) in the polycistronic cassettes (Figure 2A) reveals that pAKT levels increase with increasing $HRAS^{G12V}$ levels (Figure S5A). Therefore, we treated cells with an AKT inhibitor (AKTi) to block PI3K signaling at high levels of $HRAS^{G12V}$ (Figure S5B). At low AKTi doses, we found no improvement in proliferation or conversion; higher doses reduce cell counts, suggesting toxicity (Figures S5C–S5E). AKTi treatment fails to attenuate senescence (Figure S5E). Depending on the cellular context, JNK signaling can prevent or induce senescence.[61] We tested a JNK inhibitor (JNKi). In the RISDD condition, JNKi treatment does not attenuate senescence (Figure S5F).

When $HRAS^{G12V}$ expression is excessively high in the RISDD condition, inhibiting the MAPK pathway with MEKi effectively rescues cell-fate programming. Tuning MAPK signaling increases proliferation and reduces senescence. In contrast, inhibition of the PI3K or JNK pathways does not produce similar effects. Thus, driven by high $HRAS^{G12V}$ expression, high levels of MAPK signaling induce senescence, which can be tuned by MEKi treatment.

Activation of MAPK signaling induces high rates of conversion in the absence of mutant *RAS*

We wondered if the activation of MAPK signaling—in the absence of a *RAS* mutant—could drive high efficiency

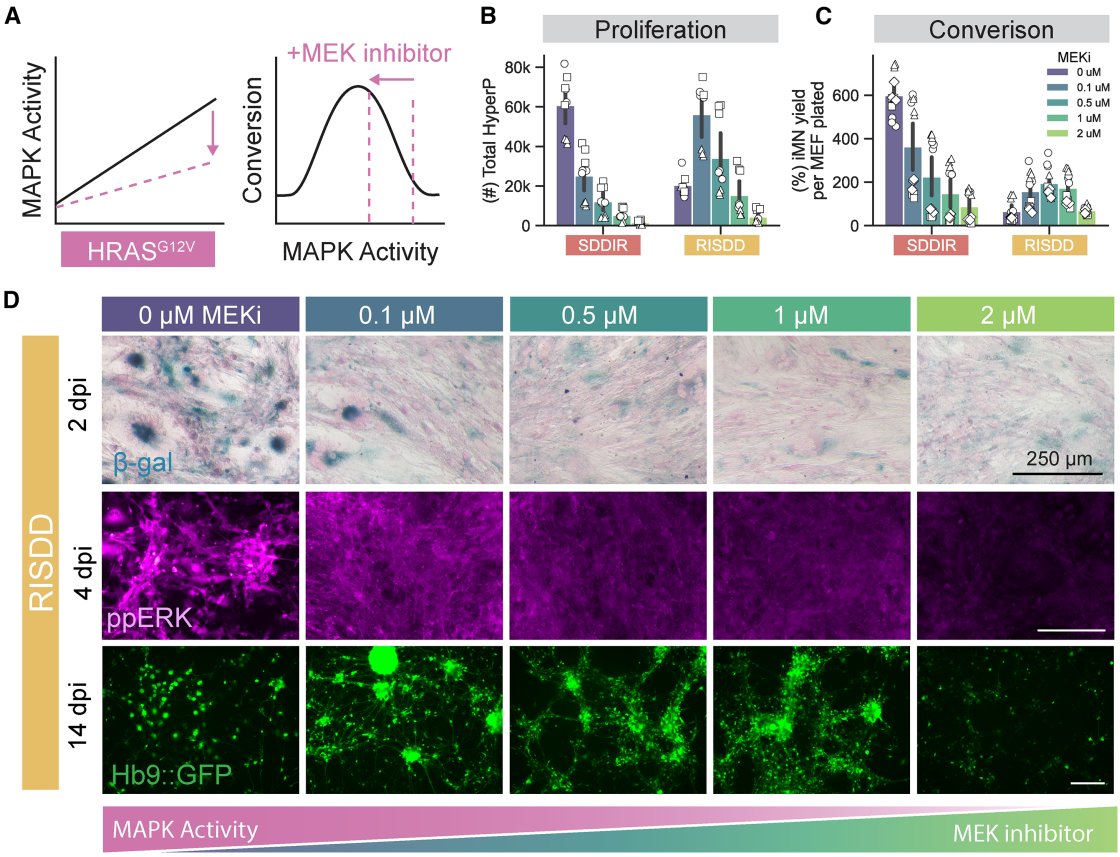

Figure 3. Tuning MAPK signaling attenuates senescence and increases conversion

(A) Diagram depicting the expected results of adding an MEK inhibitor on MAPK signaling levels and conversion.

(B) Total number of HyperP cells at 4 dpi with an MEK inhibitor (PD0325901) titration for the two polycistronic cassettes with highest *HRAS*^{G12V} expression (SDDIR and RISDD). Mean is shown with 95% confidence interval; marker style denotes biological reps; $n = 3$ biological reps per condition.

(C) Conversion yield at 14 dpi with an MEK inhibitor titration for the two polycistronic cassettes with highest *HRAS*^{G12V} expression. Mean is shown with 95% confidence interval; marker style denotes biological reps; $n = 4$ biological reps per condition.

(D) Representative images of cells stained for senescence-associated β -galactosidase (β-gal) and nuclear fast red at 2 dpi, ppERK at 4 dpi, and *Hb9::GFP* expression in iMNs at 14 dpi for the polycistronic cassette with the highest *HRAS*^{G12V} expression (RISDD) with MEKi titration. Scale bars, 250 μm.

conversion. Diverse extracellular cues, including small molecules, stimulate MAPK signaling.[62–64] Potentially, transient stimuli such as small molecules could replace the delivery of the oncogene *HRAS*^{G12V}, increasing safety and simplifying the genetic cocktail for direct conversion. The small molecule phorbol 12-myristate 13-acetate (PMA) activates protein kinase C to trigger signaling in the MAPK pathway.[1,65–67] We hypothesized that the addition of PMA to converting cells would drive direct conversion by inducing signaling and proliferation, offering an alternative to activation via oncogenic *RAS* expression (Figures 4A and 4B). Across a range of concentrations, we find that the addition of PMA increases the levels of ppERK (Figures 4C and S6A–S6D).

To explore the effects of PMA on proliferation and conversion, we treated converting cells with PMA from 1 dpi through 14 dpi. In the absence of mutant *HRAS*, PMA treatment increases both the number and percentage of HyperP cells at 4 dpi (Figures 4D, S6E, and S6F). The boost in proliferation correlates with improved iMN yield and purity (Figures 4E, S6G, and S6H). Specifically, PMA increases conversion yield by up to 5-fold. Compared with transcription factors alone, the addition of 100 nM PMA with SNAP-*DD* increases conversion yield by 120-fold, approaching 100% yield. However, PMA-converted iMNs have less mature morphology and neurite outgrowth compared with *HRAS*^{G12V}-converted cells (Figure S6D). Higher concentrations of PMA do not increase yield, and at the highest concentration, we observed lower conversion rates (Figures S6G and S6H).

If PMA and *HRAS*^{G12V} work through a shared mechanism of optimal MAPK signaling, we would expect that the addition of PMA to conditions with high *HRAS*^{G12V} would not increase the rates of proliferation or conversion. When we added PMA to converting cells with high levels of *HRAS*^{G12V}, we observed no increase in proliferation (Figures 4F, S6I, and S6J) or conversion (Figures 4G, S6K, and S6L). Rather, both metrics showed slight reductions. As PMA does not increase the rates of conversion in *HRAS*^{G12V}-expressing conditions, our results suggest that both PMA and *HRAS*^{G12V} drive conversion through MAPK signaling.

To demonstrate that PMA increases the rates of conversion by inducing MAPK signaling, we treated cells infected with NIL SNAP-*DD* with combinations of PMA and MEKi at different concentrations (Figure 4H). Low MEKi concentration partially reduces the PMA-mediated boost in conversion, while high MEKi concentration completely abolishes the boost in conversion (Figures 4I and S6M). Overall, we demonstrate that we can replace oncogenic *RAS* with a small-molecule activator of MAPK signaling to induce high rates of conversion.

MAPK signaling regulates Ngn2 levels to support proliferation-dependent iMN conversion

Beyond driving hyperproliferation, we wondered how MAPK signaling influences the conversion of MEFs to motor neurons. MAPK signaling triggers the phosphorylation of diverse transcription factors, including Oct4, Klf4, Ascl1, and Ngn2, changing their binding and stability and influencing cell fate.[68–72] Proline-directed kinases—such as cyclin-dependent kinases (CDKs)—phosphorylate Ngn2 in nine serine-proline sites.[73,74] The phosphorylation state of Ngn2 can affect stability as well as its interaction with DNA.[72,73] Hyperphosphorylated Ngn2 transiently binds to target promoters, whereas hypophosphorylated Ngn2 binds more stably, recruiting additional proteins that open the regions of closed chromatin.[73,75,76] In neural progenitor cells, Ngn2 phosphorylation maintains rapid cell cycling and progenitor maintenance, whereas reduced Ngn2 phosphorylation promotes differentiation by enhancing the transcription of neuronal genes and slowing the cell cycle (Figure 5A).[72] Given that ERK is also a proline-directed serine kinase and MAPK signaling drives cell cycle progression, we examined whether MAPK activity during conversion regulates Ngn2 function through phosphorylation.

To explore Ngn2 phosphorylation, we used a phospho-deficient mutant of *Ngn2*, termed *9SA Ngn2*, in which all nine serine-proline sites are mutated to alanine-proline, preventing phosphorylation.[73] Prior studies showed that a phospho-deficient mutant *Ngn2* increases neuronal differentiation in *Xenopus* embryos and P19 cells[72,73] and enhances neuronal maturity in direct conversion from human fibroblasts[71] and primary mouse astrocytes.[77] To test the effect of these phosphorylation sites in our high-efficiency conversion system, we compared proliferation, conversion efficiency, and Ngn2 protein expression for conversion with wild-type (WT) and *9SA Ngn2*.

Substitution of *Ngn2* for the *9SA Ngn2* mutant supported conversion, indicating that the mutant retains essential functions for conversion. However, the expression of *9SA Ngn2* significantly reduces both proliferation and iMN yield compared with WT *Ngn2*, not only in conditions with our high-efficiency cassette, RAS-IRES-p53DD (RIDD) (Figures 5B and 5C), but also across multiple other conversion conditions (Figures S7A–S7C). With *9SA Ngn2*, we observed that iMN purity is higher in conditions with low MAPK activity (e.g., without RAS or PMA, or with MEK inhibition) but unchanged in conditions with elevated MAPK signaling (e.g., with RAS or PMA; Figure S7D). Across all conditions, the *9SA* mutant consistently shows higher protein expression of the *Ngn2* transgene than WT *Ngn2* (Figures 5D, S7E, and S7F). Higher Ngn2 levels may increase binding and transcription at Ngn2 targets across sites in the genome to drive commitment to the neuronal lineage. However, the enhanced differentiation capacity of *9SA Ngn2* leads to lower total yield by prematurely slowing the cell cycle and preventing the initial proliferative phase.

To explore the effect of MAPK levels on Ngn2 levels, we measured Ngn2 levels at 4 dpi while pharmacologically altering MAPK signaling. When MAPK activity was increased with PMA, WT Ngn2 levels decreased, while 9SA levels remained unchanged (Figure 5E). Conversely, reducing MAPK activity with an MEK inhibitor increased WT Ngn2 levels, with no change in 9SA Ngn2 levels (Figure 5E). These results suggest that MAPK signaling specifically affects WT Ngn2 levels, while the phospho-deficient *9SA* mutant remains stable.

Phosphorylation can generate distinct species, which influence Ngn2's interactions with other proteins and the genome.[72,73] We wondered if MAPK signaling influences both the levels and distribution of Ngn2 phosphorylation states. Protein properties can be affected by multi-phosphorylation and ubiquitination states, which can be detected through migration through SDS-PAGE gels. In cells converting in the absence of RIDD, WT Ngn2 appeared as multiple bands, suggesting differential post-translational modification, whereas 9SA Ngn2 migrated as a single band (Figure 5F). Active MAPK signaling alters the banding pattern of WT Ngn2. As expected, the addition of RIDD reduced the overall levels of Ngn2, most substantially reducing the higher band. In the presence of RIDD, the banding pattern induced by MAPK inhibition mirrors multi-band pattern observed in the MAPK-low condition, with an increase in the higher Ngn2 band. Notably, altered MAPK activity does not affect the banding pattern of 9SA Ngn2. Together, these findings indicate that MAPK signaling influences the levels of Ngn2, putatively by generating different phosphoforms that may also influence the stability of WT Ngn2.

Overall, our data suggest that MAPK-mediated phosphorylation of WT Ngn2 promotes cell cycle progression and expansion of a conversion-receptive population. Conversely, loss of Ngn2 phosphorylation increases Ngn2 levels to promote precocious neuronal differentiation. Precocious commitment to the neuronal fate reduces conversion yield by impeding the proliferative phase.

DISCUSSION

Understanding how signaling pathways influence cell-fate transitions in healthy primary cells offers a window into development, tissue homeostasis, and disease. In this work, we demonstrate that cell-fate programming of primary cells responds biphasically to MAPK signaling. Using a combination of chemical and genetic activators to tune signaling, we find that intermediate levels of signaling promote the proliferation and conversion of primary mouse embryonic fibroblasts to motor neurons without inducing senescence. Co-expressed MAPK and *p53* mutants tune MAPK signaling to set the level optimal for proliferation and conversion. Rates of conversion vary as a function of genetic factors, such as differences in p53 activity,[51,78,79] and extrinsic features, such as the batch of virus or cells. Importantly, when we applied chemical activators and inhibitors to the MAPK pathway, we observed diverging responses that are dependent on the expression level of mutant *HRAS*. Understanding this

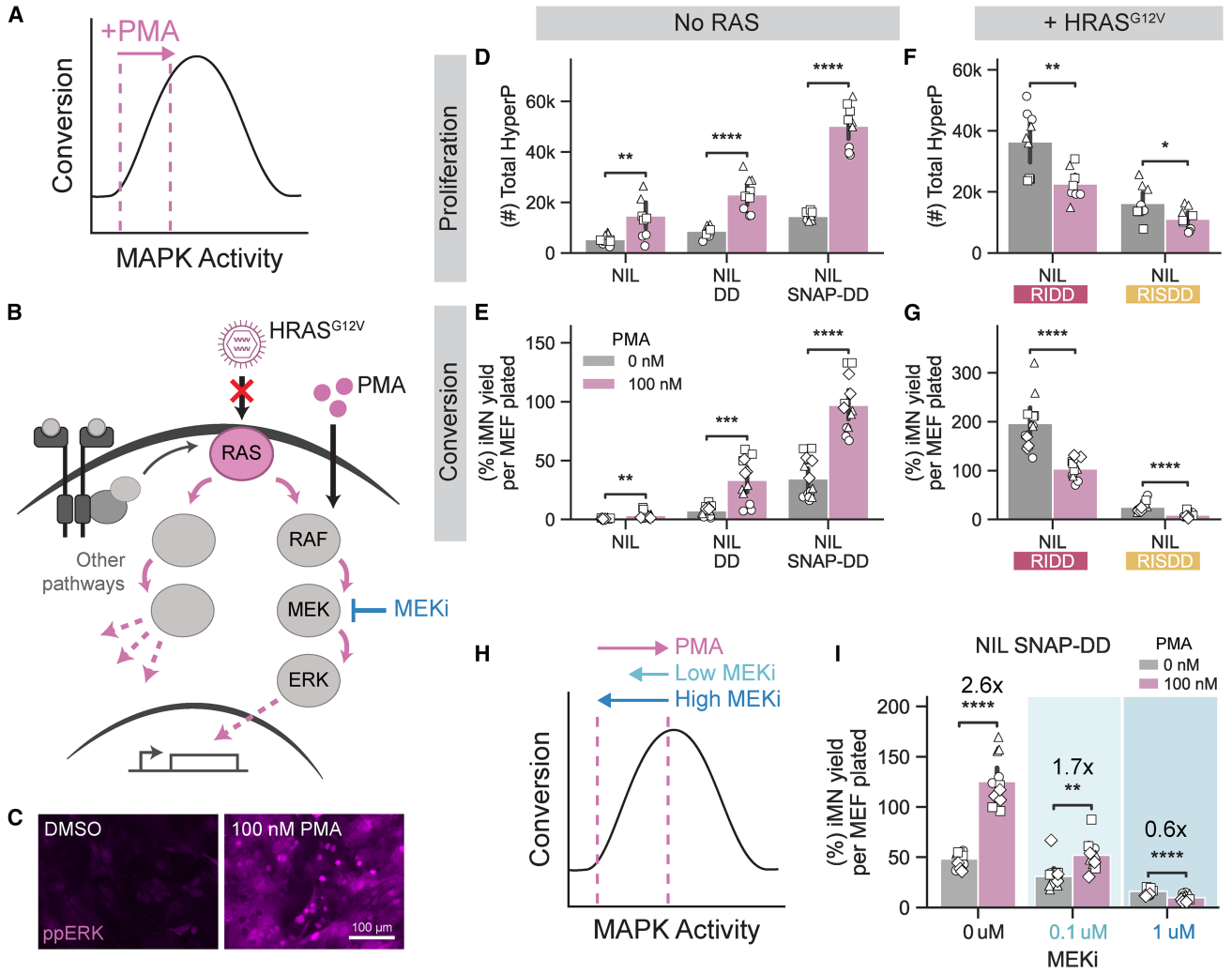

Figure 4. Activation of MAPK signaling induces high rates of conversion in the absence of mutant *RAS*

(A) Diagram depicting the expected results of adding PMA, a small-molecule activator of the MAPK pathway, on MAPK signaling levels and conversion.

(B) Schematic depicting the replacement of viral transduction of *RAS* oncogene with small-molecule PMA to activate MAPK signaling.

(C) Representative images of immunofluorescent staining for ppERK in cells fixed 20 min after treatment with either a vehicle control (DMSO) or 100 nM PMA. Scale bars, 100 μm.

(D and E) Total number of HyperP cells at 4 dpi (D) and conversion yield at 14 dpi (E) with 100 nM PMA treatment for conditions without RAS. Mean is shown with 95% confidence interval; marker style denotes biological reps; $n = 3$ or 4 biological reps per condition; t test independent samples.

(F and G) Total number of HyperP cells at 4 dpi (F) and conversion yield at 14 dpi (G) with 100 nM PMA treatment for conditions with polycistronic cassettes containing *HRAS*^{G12V}. Mean is shown with 95% confidence interval; marker style denotes biological reps; $n = 3$ or 4 biological reps per condition; t test independent samples.

(H) Diagram depicting the expected results of adding PMA in combination with an MEK inhibitor to test whether the effects of PMA are specific to the MAPK pathway.

(I) Conversion yield quantified at 14 dpi for cells infected with NIL SNAP-*DD* and treated with combinations of 0 nM or 100 nM PMA to activate MAPK signaling and 0 μM, 0.1 μM, or 1 μM of MEK inhibitor (PD0325901) to inhibit MAPK signaling. Small molecules were added to the media beginning at 1 dpi. Mean is shown with 95% confidence interval; marker style denotes biological reps; $n = 4$ biological reps per condition; t test independent samples.

Significance summary: $p > 0.05$ (ns); $^{*}p \leq 0.05$; $^{**}p \leq 0.01$; $^{***}p \leq 0.001$; and $^{****}p \leq 0.0001$.

non-monotonic landscape allowed us to maintain high rates of conversion in the absence of *HRAS*^{G12V} by supplementing with a small-molecule activator of the MAPK pathway. MAPK signaling also plays a role in the regulation of Ngn2 activity during conversion. Extending these findings to additional systems and human cells may reveal opportunities to precisely reshape signaling and selectively control cell-fate transitions, improving the precision of therapeutic interventions.

Our findings align with other studies that show that an optimal level of MAPK signaling promotes transformation and tumorigenesis.[80–82] Directly changing the expression levels of MAPK pathway mutants reveals that intermediate levels of mutant

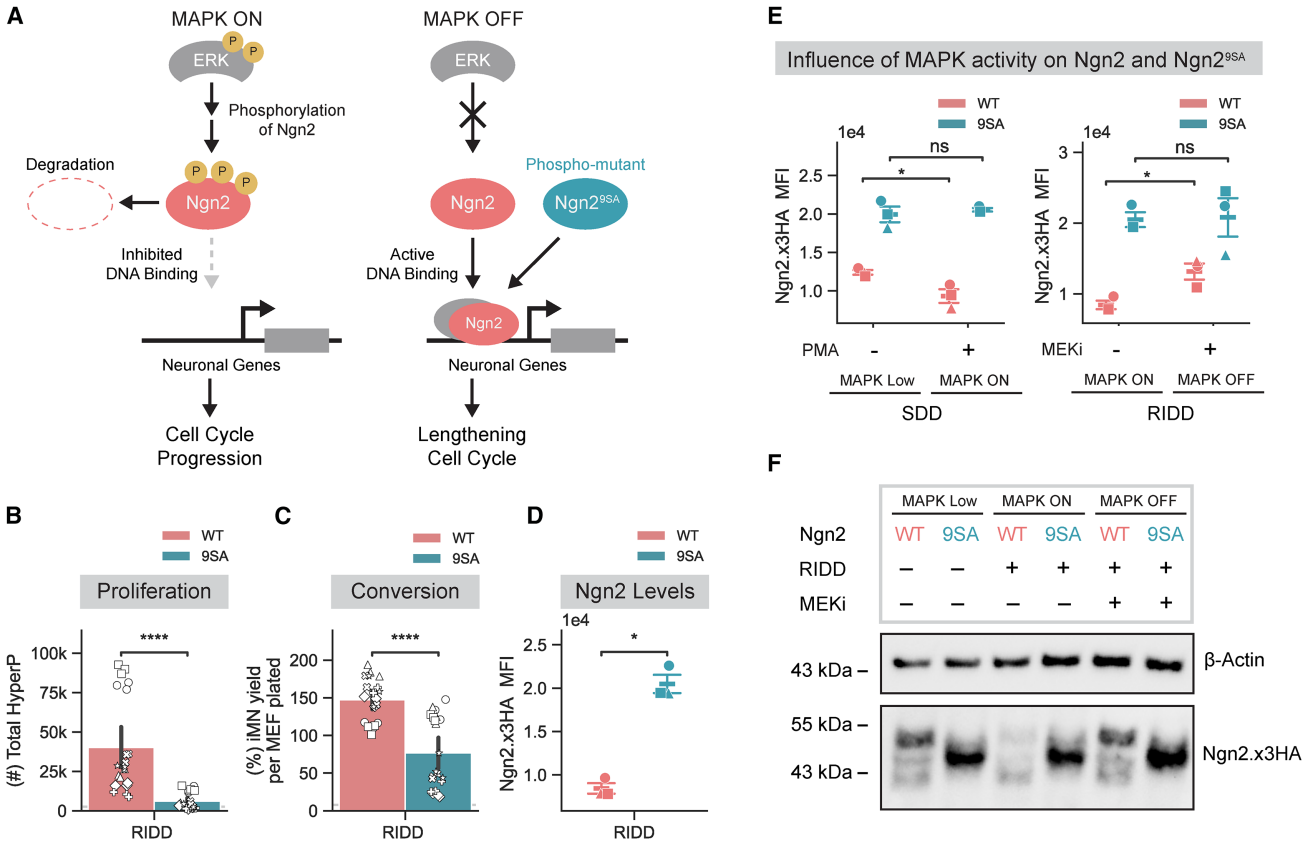

Figure 5. MAPK signaling regulates Ngn2 levels to support proliferation-dependent iMN conversion

(A) Schematic depicting the hypothesized effect of MAPK signaling on Ngn2 phosphorylation and activity.

(B and C) Total number of HyperP cells at 4 dpi (B) and conversion yield at 14 dpi (C) for cells infected with either wild-type (WT) or phospho-mutant (*9SA*) *Ngn2*, along with Isl1, Lhx3, and *HRAS*^{G12V}-IRES-*p53DD* (RIDD). Mean is shown with 95% confidence interval; marker style denotes biological reps; $n = 6$ biological reps per condition; t test independent samples.

(D) Ngn2 mean fluorescent intensity (MFI) at 4 dpi measured by immunofluorescent flow cytometry for cells infected with either WT or *9SA Ngn2* along with Isl1, Lhx3, and RIDD. Mean ± SEM is shown. Marker style denotes biological reps, $n = 3$ biological reps per condition; t test independent samples.

(E) Ngn2 levels measured at 4 dpi by immunofluorescent flow cytometry for different MAPK signaling conditions. Mean ± SEM is shown. Marker style denotes biological reps, $n = 3$ biological reps per condition; t test independent samples.

(F) Western blot of HA-tagged Ngn2 from lysate collected at 4 dpi, including β-actin as a loading control.

Significance summary: $p > 0.05$ (ns); $^{*}p \leq 0.05$; $^{**}p \leq 0.01$; $^{***}p \leq 0.001$; and $^{****}p \leq 0.0001$.

expression support proliferation.[4,52] Interestingly, we observe that the inhibition of MAPK signaling promotes survival in cells with high expression of *HRAS*^{G12V}. Attenuated signaling in the presence of high levels of *HRAS*^{G12V} limits oncogene-induced senescence. High MAPK signaling may generally drive cells to terminal fates, such as senescence or apoptosis through p53 activation. Strong MAPK pathway-activating mutations, such as in *KRAS* and *BRAF*, are mutually exclusive in cancer.[10] Simultaneous expression of these mutants is cytotoxic to cells and suppresses tumor formation.[11,12] In primary mouse embryonic fibroblasts, co-expression of hyperactive *KRAS* and *BRAF* mutants halts proliferation and causes oncogene-induced senescence.[11] Similar to our findings, the inhibition of MAPK signaling can reduce senescence and toxicity associated with oncogene overexpression.[5,12] Conversely, MAPK pathway activation may reduce proliferation and increase cell stress, leading to senescence or cell death, presenting a potential treatment strategy for cancers with hyperactive MAPK signaling.[83–85] Resistance to MAPK pathway inhibitors could be mitigated by removing the inhibitor, resulting in toxic hyperactivation of MAPK signaling.[86,87] Our findings provide a nuanced perspective on MAPK modulation that may better guide the development of tailored MAPK inhibitors for therapeutic contexts. Tools that precisely control the expression of oncogenes may support the development of genetic systems that more accurately model cell states prior to and during transformation.[88,89]

Addition of the small-molecule MAPK activator PMA allowed us to generate neurons at high rates in the absence of mutant *HRAS*. Elimination of oncogenes reduces the risk of transformation, improving the safety profile of scalably produced, *in vitro*-derived cells for translational applications such as cellular therapies. While PMA improves conversion efficiency without oncogenic *RAS*, the PMA-converted cells exhibit less mature morphologies compared with their RAS-converted counterparts

(Figure S6D). Constant stimulation of MAPK signaling may impede neurite outgrowth. In development and differentiation, the levels and dynamics of MAPK signaling impact neural differentiation and maturation.[1,90–92] By tuning the duration of PMA stimulation, we may be able to increase neuronal morphology and maturation while retaining high rates of conversion. Alternatively, PMA-converted cells may require a longer conversion timeline to mature, which can be explored through prolonged culture in the presence or absence of PMA. While the safety profile of the PMA-based protocol is an improvement over oncogenic *RAS*, more work is needed to assess the long-term stability and translational potential of PMA-converted cells.

In addition to increasing proliferation, MAPK signaling may influence conversion by regulating Ngn2 activity through phosphorylation. We observed that lower MAPK signaling levels were associated with higher WT Ngn2 levels, while levels of a phosphosite-deficient mutant *Ngn2* were unaffected. Previous work from our lab indicates that within the HyperP population, cells with higher levels of Ngn2 convert at higher rates.[31,32] Higher Ngn2 expression may compensate for reduced DNA-binding affinity when the protein is hyperphosphorylated, reflecting a key tradeoff: Ngn2 phosphorylation enables hyperproliferation, while hypophosphorylation enhances neuronal gene activation and maturation. These findings emphasize that precise coordination between cell cycle exit and neuronal commitment is essential for efficient conversion in our system, and MAPK signaling may play an important role in this process.

Beyond MAPK signaling levels, the signaling dynamics may also control differentiation. In PC12 cells, for example, transient MAPK activation promotes proliferation, whereas sustained activation induces neuronal differentiation.[1] Likewise, oscillatory Notch signaling drives fluctuating expression levels of Ngn2 in neural progenitors, while stable Ngn2 accumulation promotes differentiation.[72,93,94] Whether similar signaling dynamics operate during direct conversion remains unknown and warrants further investigation.[1]

Phosphorylation regulates another proneural transcription factor, Ascl1, which shares the basic helix–loop–helix (bHLH) structure of Ngn2.[71] Ascl1 phosphorylation is elevated in neuroblastoma and glioblastoma, where high proliferation rates are thought to prevent differentiation by maintaining Ascl1 in a hyperphosphorylated, low-activity state.[95–97] In contrast, the expression of phospho-mutant *Ascl1* in these tumor cells promotes differentiation and cell cycle exit,[95–97] which parallels our observations with phospho-mutant *Ngn2*. Interestingly, although our conversion system includes oncogenic drivers, the presence of these mitotic drivers does not impede conversion to a post-mitotic identity. The exact context or timing of MAPK activation may be key for routing cells efficiently through cell-fate transitions. Indeed, prior studies have shown that MAPK signaling levels influence the fate of neural precursors, where low MAPK activity supports neurogenesis, while high levels promote gliogenesis.[97–99]

In summary, $HRAS^{G12V}$ can drive cells to a state receptive to conversion by promoting proliferation through MAPK signaling. However, extremely high expression levels of mutant *RAS* lead to oncogene-induced senescence. This tradeoff between proliferation and senescence results in a biphasic correlation between $HRAS^{G12V}$ expression and conversion. We can direct cells through MAPK signaling regimes by genetically tuning $HRAS^{G12V}$ levels or via small-molecule interventions. In addition, MAPK signaling may influence the ability of Ngn2 to induce conversion. Overall, our work underscores the critical role of fine-tuning MAPK signaling during cell-fate transitions.

Limitations of the study

Although PMA enhances conversion efficiency without requiring the expression of oncogenic *RAS*, the resulting PMA-converted cells display less mature morphologies than those generated with *RAS*. Both $HRAS^{G12V}$ and PMA improve conversion through MAPK pathway activation, yet their distinct effects suggest opportunities to explore additional MAPK modulators to increase cell yields and morphological maturity. While $HRAS^{G12V}$ effectively drives the conversion of MEFs to iMNs, $HRAS^{G12V}$ fails to support the conversion of adult human fibroblasts to neurons.[32] The addition of *myr-AKT*, *BCL2*, and *c-MYC* with NIL and *p53DD* in primary adult human fibroblasts increases the rates of conversion.[32] Notably, *AKT* and *MYC* are both activated downstream of RAS signaling, suggesting that species-specific signaling patterns may differentiate the effects of mutant *RAS* on mouse and human cells. *RAS* isoforms differ in their mutation frequency and endogenous expression levels across human cancers. *KRAS* is the most frequently mutated isoform, followed by *NRAS* and *HRAS*.[8,100] Other *RAS* mutants may have different optimal expression levels based on their transforming potential and cell context.[46] Differences in the response of adult human fibroblasts and mouse embryonic fibroblasts to $HRAS^{G12V}$ may reflect a distinct window of sensitivity to RAS levels, species-specific disparities, or differences in the developmental stage of the initial cells. Investigating these differences could shed light on molecular requirements for the conversion of human cells and pave the way for improved protocols.

RESOURCE AVAILABILITY

Lead contact

Requests for further information and resources should be directed to and will be fulfilled by the lead contact, Kate E. Galloway, PhD (katiegal@mit.edu).

Materials availability

Plasmids generated in this study have been deposited to Addgene.

Data and code availability

- The RNA-seq data discussed in this publication have been deposited in NCBI's Gene Expression Omnibus and are accessible through GEO Series accession number GEO: GSE303587.
- Other data (e.g., flow cytometry data) have been deposited at Zenodo (https://doi.org/10.5281/zenodo.16576807).
- Code is available at https://github.com/GallowayLabMIT/article-MAPK-chemogenetic-tuning (https://doi.org/10.5281/zenodo.16739843).
- Any additional information required to reanalyze the data reported in this paper is available from the lead contact upon request.

ACKNOWLEDGMENTS

Research reported in this manuscript was supported by the National Institute of General Medical Sciences of the National Institutes of Health under award no. R35-GM143033, by the National Science Foundation under the NSF-CAREER under award no. 2339986, and with funding from the Institute for Collaborative Biotechnologies under cooperative agreement W911NF-19-2-0026. B.A.L.-D.

is supported by the National Science Foundation Graduate Research Fellowship Program under grant no. 1745302. We thank the Koch Institute's Robert A. Swanson (1969) Biotechnology Center (National Cancer Institute Grant P30-CA14051) for technical support, specifically the Flow Cytometry Core and the BioMicro Center Core facilities. We would also like to acknowledge the MIT Office of Research Computing and Data for providing high performance computing resources that were used for the analysis of the RNA sequencing results reported within this paper. We thank Adam Beitz and Christopher Johnstone for their guidance on RNA sequencing. We thank Emma Peterman, Sneha Kabaria, Kasey Love, Adam Beitz, and Mary Ehmann for feedback on the manuscript.

AUTHOR CONTRIBUTIONS

B.A.L.-D. and K.E.G. conceived and outlined the project. B.A.L.-D. cloned DD RAS polycistronic cassette retrovirus plasmids and mRuby2-RAS and TagBFP lentivirus plasmids. B.A.L.-D., J.C.A., and Y.B. performed conversion experiments and analyzed data. B.A.L.-D. and J.C.A. performed immunofluorescent staining. B.A.L.-D. performed western blots and senescence staining. B.A.L.-D. performed RNA extraction and sequencing analysis. B.A.L.-D. and K.E.G. wrote the manuscript. K.E.G. supervised the project.

DECLARATION OF INTERESTS

The authors declare no competing interests.

STAR★METHODS

Detailed methods are provided in the online version of this paper and include the following:

- KEY RESOURCES TABLE
- EXPERIMENTAL MODEL AND STUDY PARTICIPANT DETAILS
  - Cell lines and tissue culture
  - MEF dissection and isolation
- METHOD DETAILS
  - Plasmid construction
  - Retroviral transduction and conversion of MEFs to iMNs
  - Lentiviral production in HEK293Ts
  - Functional titer measurement and quantification
  - Lentiviral transduction of MEFs
  - Twin plate conversion assay
  - Conversion with signaling pathway inhibitors and PMA
  - CellTrace proliferation assay
  - Flow cytometry
  - Fixation and immunofluorescent staining
  - Immunofluorescent staining for flow cytometry
  - Senescence-associated β-galactosidase staining
  - Western blot
  - Bulk RNA sequencing
- QUANTIFICATION AND STATISTICAL ANALYSIS

SUPPLEMENTAL INFORMATION

Supplemental information can be found online at https://doi.org/10.1016/j.celrep.2025.116226.

Received: January 27, 2025
Revised: July 2, 2025
Accepted: August 11, 2025

REFERENCES

1. Santos, S.D.M., Verveer, P.J., and Bastiaens, P.I.H. (2007). Growth factor-induced MAPK network topology shapes Erk response determining PC-12 cell fate. Nat. Cell Biol. *9*, 324–330.
2. Galloway, K.E., Franco, E., and Smolke, C.D. (2013). Dynamically Reshaping Signaling Networks to Program Cell Fate via Genetic Controllers. Science *341*, 1235005.
3. Hamilton, W.B., Mosesson, Y., Monteiro, R.S., Emdal, K.B., Knudsen, T. E., Francavilla, C., Barkai, N., Olsen, J.V., and Brickman, J.M. (2019). Dynamic lineage priming is driven via direct enhancer regulation by ERK. Nature *575*, 355–360.
4. Chen, J.-Y., Hug, C., Reyes, J., Tian, C., Gerosa, L., Fröhlich, F., Ponsioen, B., Snippert, H.J.G., Spencer, S.L., Jambhekar, A., et al. (2023). Multi-range ERK responses shape the proliferative trajectory of single cells following oncogene induction. Cell Rep. *42*, 112252.
5. Nieto, P., Ambrogio, C., Esteban-Burgos, L., Gómez-López, G., Blasco, M.T., Yao, Z., Marais, R., Rosen, N., Chiarle, R., Pisano, D.G., et al. (2017). A Braf kinase-inactive mutant induces lung adenocarcinoma. Nature *548*, 239–243.
6. Lau, K.S., Juchheim, A.M., Cavaliere, K.R., Philips, S.R., Lauffenburger, D.A., and Haigis, K.M. (2011). In Vivo Systems Analysis Identifies Spatial and Temporal Aspects of the Modulation of TNF-α–Induced Apoptosis and Proliferation by MAPKs. Sci. Signal. *4*, ra16.
7. Sanchez-Vega, F., Mina, M., Armenia, J., Chatila, W.K., Luna, A., La, K. C., Dimitriadoy, S., Liu, D.L., Kantheti, H.S., Saghafinia, S., et al. (2018). Oncogenic Signaling Pathways in The Cancer Genome Atlas. Cell *173*, 321–337.e10.
8. Hobbs, G.A., Der, C.J., and Rossman, K.L. (2016). RAS isoforms and mutations in cancer at a glance. J. Cell Sci. *129*, 1287–1292.
9. McCubrey, J.A., Steelman, L.S., Chappell, W.H., Abrams, S.L., Montalto, G., Cervello, M., Nicoletti, F., Fagone, P., Malaponte, G., Mazzarino, M. C., et al. (2012). Mutations and Deregulation of Ras/Raf/MEK/ERK and PI3K/PTEN/Akt/mTOR Cascades Which Alter Therapy Response. Oncotarget *3*, 954–987.
10. Cisowski, J., and Bergo, M.O. (2017). What makes oncogenes mutually exclusive? Small GTPases *8*, 187–192.
11. Cisowski, J., Sayin, V.I., Liu, M., Karlsson, C., and Bergo, M.O. (2016). Oncogene-induced senescence underlies the mutual exclusive nature of oncogenic KRAS and BRAF. Oncogene *35*, 1328–1333.
12. Unni, A.M., Harbourne, B., Oh, M.H., Wild, S., Ferrarone, J.R., Lockwood, W.W., and Varmus, H. (2018). Hyperactivation of ERK by multiple mechanisms is toxic to RTK-RAS mutation-driven lung adenocarcinoma cells. eLife *7*, e33718.
13. Ying, Q.-L., Wray, J., Nichols, J., Batlle-Morera, L., Doble, B., Woodgett, J., Cohen, P., and Smith, A. (2008). The ground state of embryonic stem cell self-renewal. Nature *453*, 519–523.
14. Goglia, A.G., Wilson, M.Z., Jena, S.G., Silbert, J., Basta, L.P., Devenport, D., and Toettcher, J.E. (2020). A Live-Cell Screen for Altered Erk Dynamics Reveals Principles of Proliferative Control. Cell Syst. *10*, 240–253.e6.
15. Ingolia, N.T., and Murray, A.W. (2007). Positive-Feedback Loops as a Flexible Biological Module. Curr. Biol. *17*, 668–677.
16. Bashor, C.J., Helman, N.C., Yan, S., and Lim, W.A. (2008). Using Engineered Scaffold Interactions to Reshape MAP Kinase Pathway Signaling Dynamics. Science *319*, 1539–1543.
17. Bugaj, L.J., Sabnis, A.J., Mitchell, A., Garbarino, J.E., Toettcher, J.E., Bivona, T.G., and Lim, W.A. (2018). Cancer mutations and targeted drugs can disrupt dynamic signal encoding by the Ras-Erk pathway. Science *361*, eaao3048.
18. Harmange, G., Hueros, R.A.R., Schaff, D.L., Emert, B., Saint-Antoine, M., Kim, L.C., Niu, Z., Nellore, S., Fane, M.E., Alicea, G.M., et al. (2023). Disrupting cellular memory to overcome drug resistance. Nat. Commun. *14*, 7130.
19. Jain, N., Goyal, Y., Dunagin, M.C., Cote, C.J., Mellis, I.A., Emert, B., Jiang, C.L., Dardani, I.P., Reffsin, S., Arnett, M., et al. (2024). Retrospective identification of cell-intrinsic factors that mark pluripotency potential in rare somatic cells. Cell Syst. *15*, 109–133.e10.

20. Wilson, M.Z., Ravindran, P.T., Lim, W.A., and Toettcher, J.E. (2017). Tracing Information Flow from Erk to Target Gene Induction Reveals Mechanisms of Dynamic and Combinatorial Control. Mol. Cell *67*, 757–769.e5.

21. Takahashi, K., and Yamanaka, S. (2006). Induction of Pluripotent Stem Cells from Mouse Embryonic and Adult Fibroblast Cultures by Defined Factors. Cell *126*, 663–676.

22. Papapetrou, E.P., Tomishima, M.J., Chambers, S.M., Mica, Y., Reed, E., Menon, J., Tabar, V., Mo, Q., Studer, L., and Sadelain, M. (2009). Stoichiometric and temporal requirements of Oct4, Sox2, Klf4, and c-Myc expression for efficient human iPSC induction and differentiation. Proc. Natl. Acad. Sci. USA *106*, 12759–12764.

23. Wernig, M., Meissner, A., Cassady, J.P., and Jaenisch, R. (2008). c-Myc Is Dispensable for Direct Reprogramming of Mouse Fibroblasts. Cell Stem Cell *2*, 10–12.

24. Wu, Q., Zhang, J., Long, B., Hu, X., de Faria, B.M., Scalf, S.M., Karatepe, K., Cao, W., Tsopoulidis, N., Binkercosen, A., et al. (2024). Morphomechanic tuning of ERK by actin-TFII-IΔ regulates cell identity. Preprint at bioRxiv. https://doi.org/10.1101/2023.06.02.543427.

25. Kunath, T., Saba-El-Leil, M.K., Almousailleakh, M., Wray, J., Meloche, S., and Smith, A. (2007). FGF stimulation of the Erk1/2 signalling cascade triggers transition of pluripotent embryonic stem cells from self-renewal to lineage commitment. Development *134*, 2895–2902.

26. Stavridis, M.P., Lunn, J.S., Collins, B.J., and Storey, K.G. (2007). A discrete period of FGF-induced Erk1/2 signalling is required for vertebrate neural specification. Development *134*, 2889–2894.

27. Nett, I.R., Mulas, C., Gatto, L., Lilley, K.S., and Smith, A. (2018). Negative feedback via RSK modulates Erk-dependent progression from naïve pluripotency. EMBO Rep. *19*, e45642.

28. Chen, H., Guo, R., Zhang, Q., Guo, H., Yang, M., Wu, Z., Gao, S., Liu, L., and Chen, L. (2015). Erk signaling is indispensable for genomic stability and self-renewal of mouse embryonic stem cells. Proc. Natl. Acad. Sci. USA *112*, E5936–E5943.

29. Mayor-Ruiz, C., Olbrich, T., Drosten, M., Lecona, E., Vega-Sendino, M., Ortega, S., Dominguez, O., Barbacid, M., Ruiz, S., and Fernandez-Capetillo, O. (2018). ERF deletion rescues RAS deficiency in mouse embryonic stem cells. Genes Dev. *32*, 568–576.

30. Babos, K.N., Galloway, K.E., Kisler, K., Zitting, M., Li, Y., Shi, Y., Quintino, B., Chow, R.H., Zlokovic, B.V., and Ichida, J.K. (2019). Mitigating Antagonism between Transcription and Proliferation Allows Near-Deterministic Cellular Reprogramming. Cell Stem Cell *25*, 486–500.e9.

31. Wang, N.B., Lende-Dorn, B.A., Beitz, A.M., Han, P., Adewumi, H.O., O'Shea, T.M., and Galloway, K.E. (2025). Proliferation history and transcription factor levels drive direct conversion to motor neurons. Cell Syst. *16*, 101205. https://doi.org/10.1016/j.cels.2025.101205.

32. Wang, N.B., Adewumi, H.O., Lende-Dorn, B.A., Beitz, A.M., O'Shea, T. M., and Galloway, K.E. (2025). Compact transcription factor cassettes generate functional, engraftable motor neurons by direct conversion. Cell Syst. *16*, 101206. https://doi.org/10.1016/j.cels.2025.101206.

33. Beitz, A., Teves, J., Oakes, C., Johnstone, C., Wang, N., Brickman, J.M., and Galloway, K.E. (2024). Cells transit through a quiescent-like state to convert to neurons at high rates. Preprint at bioRxiv. https://doi.org/10.1101/2024.11.22.624928.

34. Desai, R.V., Chen, X., Martin, B., Chaturvedi, S., Hwang, D.W., Li, W., Yu, C., Ding, S., Thomson, M., Singer, R.H., et al. (2021). A DNA-repair pathway can affect transcriptional noise to promote cell fate transitions. Science *373*, eabc6506.

35. Hanna, J., Saha, K., Pando, B., van Zon, J., Lengner, C.J., Creyghton, M. P., van Oudenaarden, A., and Jaenisch, R. (2009). Direct cell reprogramming is a stochastic process amenable to acceleration. Nature *462*, 595–601.

36. Guo, S., Zi, X., Schulz, V.P., Cheng, J., Zhong, M., Koochaki, S.H.J., Megyola, C.M., Pan, X., Heydari, K., Weissman, S.M., et al. (2014). Nonstochastic Reprogramming from a Privileged Somatic Cell State. Cell *156*, 649–662.

37. Yamanaka, S. (2009). Elite and stochastic models for induced pluripotent stem cell generation. Nature *460*, 49–52.

38. Ravindran, P.T., McFann, S., Thornton, R.H., and Toettcher, J.E. (2022). A synthetic gene circuit for imaging-free detection of signaling pulses. Cell Syst. *13*, 131–142.e13.

39. Lahav, G., Rosenfeld, N., Sigal, A., Geva-Zatorsky, N., Levine, A.J., Elowitz, M.B., and Alon, U. (2004). Dynamics of the p53-Mdm2 feedback loop in individual cells. Nat. Genet. *36*, 147–150.

40. Shakiba, N., Fahmy, A., Jayakumaran, G., McGibbon, S., David, L., Trcka, D., Elbaz, J., Puri, M.C., Nagy, A., van der Kooy, D., et al. (2019). Cell competition during reprogramming gives rise to dominant clones. Science *364*, eaan0925.

41. Son, E.Y., Ichida, J.K., Wainger, B.J., Toma, J.S., Rafuse, V.F., Woolf, C. J., and Eggan, K. (2011). Conversion of mouse and human fibroblasts into functional spinal motor neurons. Cell Stem Cell *9*, 205–218.

42. Ichida, J.K., Staats, K.A., Davis-Dusenbery, B.N., Clement, K., Galloway, K.E., Babos, K.N., Shi, Y., Son, E.Y., Kiskinis, E., Atwater, N., et al. (2018). Comparative genomic analysis of embryonic, lineage-converted and stem cell-derived motor neurons. Development *145*, dev168617.

43. Hong, H., Takahashi, K., Ichisaka, T., Aoi, T., Kanagawa, O., Nakagawa, M., Okita, K., and Yamanaka, S. (2009). Suppression of induced pluripotent stem cell generation by the p53–p21 pathway. Nature *460*, 1132–1135.

44. Ruiz, S., Panopoulos, A.D., Herrerías, A., Bissig, K.D., Lutz, M., Berggren, W.T., Verma, I.M., and Izpisua Belmonte, J.C. (2011). A High Proliferation Rate Is Required for Cell Reprogramming and Maintenance of Human Embryonic Stem Cell Identity. Curr. Biol. *21*, 45–52.

45. Utikal, J., Polo, J.M., Stadtfeld, M., Maherali, N., Kulalert, W., Walsh, R. M., Khalil, A., Rheinwald, J.G., and Hochedlinger, K. (2009). Immortalization eliminates a roadblock during cellular reprogramming into iPS cells. Nature *460*, 1145–1148.

46. Muñoz-Maldonado, C., Zimmer, Y., and Medová, M. (2019). A Comparative Analysis of Individual RAS Mutations in Cancer Biology. Front. Oncol. *9*, 1088.

47. van den Akker, G.G.H., Zacchini, F., Housmans, B.A.C., van der Vloet, L., Caron, M.M.J., Montanaro, L., and Welting, T.J.M. (2021). Current Practice in Bicistronic IRES Reporter Use: A Systematic Review. Int. J. Mol. Sci. *22*, 5193.

48. Lanz, M.C., Zatulovskiy, E., Swaffer, M.P., Zhang, L., Ilerten, I., Zhang, S., You, D.S., Marinov, G., McAlpine, P., Elias, J.E., and Skotheim, J.M. (2022). Increasing cell size remodels the proteome and promotes senescence. Mol. Cell *82*, 3255–3269.e8.

49. Liu, X.L., Ding, J., and Meng, L.H. (2018). Oncogene-induced senescence: a double edged sword in cancer. Acta Pharmacol. Sin. *39*, 1553–1558.

50. Rattanavirotkul, N., Kirschner, K., and Chandra, T. (2021). Induction and transmission of oncogene-induced senescence. Cell. Mol. Life Sci. *78*, 843–852.

51. Serrano, M., Lin, A.W., McCurrach, M.E., Beach, D., and Lowe, S.W. (1997). Oncogenic ras Provokes Premature Cell Senescence Associated with Accumulation of p53 and p16INK4a. Cell *88*, 593–602.

52. Sarkisian, C.J., Keister, B.A., Stairs, D.B., Boxer, R.B., Moody, S.E., and Chodosh, L.A. (2007). Dose-dependent oncogene-induced senescence in vivo and its evasion during mammary tumorigenesis. Nat. Cell Biol. *9*, 493–505.

53. Niihori, T., Aoki, Y., Okamoto, N., Kurosawa, K., Ohashi, H., Mizuno, S., Kawame, H., Inazawa, J., Ohura, T., Arai, H., et al. (2011). HRAS mutants identified in Costello syndrome patients can induce cellular senescence: possible implications for the pathogenesis of Costello syndrome. J. Hum. Genet. *56*, 707–715.

54. Santoriello, C., Deflorian, G., Pezzimenti, F., Kawakami, K., Lanfrancone, L., d'Adda di Fagagna, F., and Mione, M. (2009). Expression of H-RASV12 in a zebrafish model of Costello syndrome causes cellular senescence in adult proliferating cells. Dis. Model. Mech. *2*, 56–67.

55. Collado, M., Gil, J., Efeyan, A., Guerra, C., Schuhmacher, A.J., Barradas, M., Benguría, A., Zaballos, A., Flores, J.M., Barbacid, M., et al. (2005). Senescence in premalignant tumours. Nature *436*, 642.

56. Di Micco, R., Fumagalli, M., Cicalese, A., Piccinin, S., Gasparini, P., Luise, C., Schurra, C., Garre', M., Nuciforo, P.G., Bensimon, A., et al. (2006). Oncogene-induced senescence is a DNA damage response triggered by DNA hyper-replication. Nature *444*, 638–642.

57. Mason, D.X., Jackson, T.J., and Lin, A.W. (2004). Molecular signature of oncogenic ras-induced senescence. Oncogene *23*, 9238–9246.

58. Gorgoulis, V., Adams, P.D., Alimonti, A., Bennett, D.C., Bischof, O., Bishop, C., Campisi, J., Collado, M., Evangelou, K., Ferbeyre, G., et al. (2019). Cellular Senescence: Defining a Path Forward. Cell *179*, 813–827.

59. Hernandez-Segura, A., Nehme, J., and Demaria, M. (2018). Hallmarks of Cellular Senescence. Trends Cell Biol. *28*, 436–453.

60. Bowman, T., Symonds, H., Gu, L., Yin, C., Oren, M., and Van Dyke, T. (1996). Tissue-specific inactivation of p53 tumor suppression in the mouse. Genes Dev. *10*, 826–835.

61. Tournier, C. (2013). The 2 Faces of JNK Signaling in Cancer. Genes Cancer *4*, 397–400.

62. Katz, M., Amit, I., and Yarden, Y. (2007). Regulation of MAPKs by growth factors and receptor tyrosine kinases. Biochim. Biophys. Acta *1773*, 1161–1176.

63. Cargnello, M., and Roux, P.P. (2011). Activation and Function of the MAPKs and Their Substrates, the MAPK-Activated Protein Kinases. Microbiol. Mol. Biol. Rev. *75*, 50–83.

64. Zhang, W., and Liu, H.T. (2002). MAPK signal pathways in the regulation of cell proliferation in mammalian cells. Cell Res. *12*, 9–18.

65. Leontieva, O.V., and Blagosklonny, M.V. (2014). Tumor promoter-induced cellular senescence: cell cycle arrest followed by geroconversion. Oncotarget *5*, 12715–12727.

66. Kolch, W., Heidecker, G., Kochs, G., Hummel, R., Vahidi, H., Mischak, H., Finkenzeller, G., Marmé, D., and Rapp, U.R. (1993). Protein kinase Cα activates RAF-1 by direct phosphorylation. Nature *364*, 249–252.

67. Ueda, Y., Hirai, S.i., Osada, S.i., Suzuki, A., Mizuno, K., and Ohno, S. (1996). Protein Kinase C δ Activates the MEK-ERK Pathway in a Manner Independent of Ras and Dependent on Raf. J. Biol. Chem. *271*, 23512–23519.

68. Kim, M.O., Kim, S.H., Cho, Y.Y., Nadas, J., Jeong, C.H., Yao, K., Kim, D. J., Yu, D.H., Keum, Y.S., Lee, K.Y., et al. (2012). ERK1 and ERK2 regulate embryonic stem cell self-renewal through phosphorylation of Klf4. Nat. Struct. Mol. Biol. *19*, 283–290.

69. Brumbaugh, J., Hou, Z., Russell, J.D., Howden, S.E., Yu, P., Ledvina, A. R., Coon, J.J., and Thomson, J.A. (2012). Phosphorylation regulates human OCT4. Proc. Natl. Acad. Sci. USA *109*, 7162–7168.

70. Dhaliwal, N.K., Miri, K., Davidson, S., Tamim El Jarkass, H., and Mitchell, J.A. (2018). KLF4 Nuclear Export Requires ERK Activation and Initiates Exit from Naive Pluripotency. Stem Cell Rep. *10*, 1308–1323.

71. Ali, F.R., Cheng, K., Kirwan, P., Metcalfe, S., Livesey, F.J., Barker, R.A., and Philpott, A. (2014). The phosphorylation status of Ascl1 is a key determinant of neuronal differentiation and maturation in vivo and in vitro. Development *141*, 2216–2224.

72. Hindley, C., Ali, F., McDowell, G., Cheng, K., Jones, A., Guillemot, F., and Philpott, A. (2012). Post-translational modification of Ngn2 differentially affects transcription of distinct targets to regulate the balance between progenitor maintenance and differentiation. Development *139*, 1718–1723.

73. Ali, F., Hindley, C., McDowell, G., Deibler, R., Jones, A., Kirschner, M., Guillemot, F., and Philpott, A. (2011). Cell cycle-regulated multi-site phosphorylation of Neurogenin 2 coordinates cell cycling with differentiation during neurogenesis. Development *138*, 4267–4277.

74. Ma, Y.-C., Song, M.R., Park, J.P., Henry Ho, H.Y., Hu, L., Kurtev, M.V., Zieg, J., Ma, Q., Pfaff, S.L., and Greenberg, M.E. (2008). Regulation of Motor Neuron Specification by GSK3-Mediated Phosphorylation of Neurogenin 2. Neuron *58*, 65–77.

75. Koyano-Nakagawa, N., Wettstein, D., and Kintner, C. (1999). Activation of Xenopus Genes Required for Lateral Inhibition and Neuronal Differentiation during Primary Neurogenesis. Mol. Cell. Neurosci. *14*, 327–339.

76. Seo, S., Richardson, G.A., and Kroll, K.L. (2005). The SWI/SNF chromatin remodeling protein Brg1 is required for vertebrate neurogenesis and mediates transactivation of Ngn and NeuroD. Development *132*, 105–115.

77. Pereira, A., Diwakar, J., Masserdotti, G., Beşkardeş, S., Simon, T., So, Y., Martín-Loarte, L., Bergemann, F., Vasan, L., Schauer, T., et al. (2024). Direct neuronal reprogramming of mouse astrocytes is associated with multiscale epigenome remodeling and requires Yy1. Nat. Neurosci. *27*, 1260–1273.

78. Morton, J.P., Timpson, P., Karim, S.A., Ridgway, R.A., Athineos, D., Doyle, B., Jamieson, N.B., Oien, K.A., Lowy, A.M., Brunton, V.G., et al. (2010). Mutant p53 drives metastasis and overcomes growth arrest/senescence in pancreatic cancer. Proc. Natl. Acad. Sci. USA *107*, 246–251.

79. Li, S., and Counter, C.M. (2021). Signaling levels mold the RAS mutation tropism of urethane. eLife *10*, e67172.

80. Li, S., Balmain, A., and Counter, C.M. (2018). A model for RAS mutation patterns in cancers: finding the sweet spot. Nat. Rev. Cancer *18*, 767–777.

81. Deschênes-Simard, X., Malleshaiah, M., and Ferbeyre, G. (2024). Extracellular Signal-Regulated Kinases: One Pathway, Multiple Fates. Cancers *16*, 95.

82. Amin, A.D., Rajan, S.S., Groysman, M.J., Pongtornpipat, P., and schatz, J.H. (2015). Oncogene Overdose: Too Much of a Bad Thing for Oncogene-Addicted Cancer Cells. Biomark Cancer *7*, BIC.S29326.

83. Dias, M.H., Friskes, A., Wang, S., Fernandes Neto, J.M., van Gemert, F., Mourragui, S., Papagianni, C., Kuiken, H.J., Mainardi, S., Alvarez-Villanueva, D., et al. (2024). Paradoxical activation of oncogenic signaling as a cancer treatment strategy. Cancer Discov. *14*, 1276–1301. https://doi.org/10.1158/2159-8290.CD-23-0216.

84. Wang, L., Lankhorst, L., and Bernards, R. (2022). Exploiting senescence for the treatment of cancer. Nat. Rev. Cancer *22*, 340–355.

85. Kazi, A., Xiang, S., Yang, H., Delitto, D., Trevino, J., Jiang, R.H.Y., Ayaz, M., Lawrence, H.R., Kennedy, P., and Sebti, S.M. (2018). GSK3 suppression upregulates β-catenin and c-Myc to abrogate KRas-dependent tumors. Nat. Commun. *9*, 5154.

86. Das Thakur, M., Salangsang, F., Landman, A.S., Sellers, W.R., Pryer, N. K., Levesque, M.P., Dummer, R., McMahon, M., and Stuart, D.D. (2013). Modelling vemurafenib resistance in melanoma reveals a strategy to forestall drug resistance. Nature *494*, 251–255.

87. Ito, T., Young, M.J., Li, R., Jain, S., Wernitznig, A., Krill-Burger, J.M., Lemke, C.T., Monducci, D., Rodriguez, D.J., Chang, L., et al. (2021). Paralog knockout profiling identifies DUSP4 and DUSP6 as a digenic dependence in MAPK pathway-driven cancers. Nat. Genet. *53*, 1664–1672.

88. Kabaria, S.R., Bae, Y., Ehmann, M.E., Beitz, A.M., Lende-Dorn, B.A., Peterman, E.L., Love, K.S., Ploessl, D.S., and Galloway, K.E. (2024). Programmable promoter editing for precise control of transgene expression. Preprint at bioRxiv. https://doi.org/10.1101/2024.06.19.599813.

89. Love, K.S., Johnstone, C.P., Peterman, E.L., Gaglione, S., Birnbaum, M. E., and Galloway, K.E. (2025). Model-guided design of microRNA-based gene circuits supports precise dosage of transgenic cargoes into diverse primary cells. Cell Syst. *16*, 101269.

90. Schmid, R.-S., Pruitt, W.M., and Maness, P.F. (2000). A MAP Kinase-Signaling Pathway Mediates Neurite Outgrowth on L1 and Requires Src-Dependent Endocytosis. J. Neurosci. *20*, 4177–4188.

91. Newbern, J.M., Li, X., Shoemaker, S.E., Zhou, J., Zhong, J., Wu, Y., Bonder, D., Hollenback, S., Coppola, G., Geschwind, D.H., et al. (2011). Specific Functions for ERK/MAPK Signaling during PNS Development. Neuron *69*, 91–105.

92. Soundararajan, P., Fawcett, J.P., and Rafuse, V.F. (2010). Guidance of Postural Motoneurons Requires MAPK/ERK Signaling Downstream of Fibroblast Growth Factor Receptor 1. J. Neurosci. *30*, 6595–6606.

93. Shimojo, H., Ohtsuka, T., and Kageyama, R. (2008). Oscillations in Notch Signaling Regulate Maintenance of Neural Progenitors. Neuron *58*, 52–64.

94. Kageyama, R., Ohtsuka, T., Shimojo, H., and Imayoshi, I. (2008). Dynamic Notch signaling in neural progenitor cells and a revised view of lateral inhibition. Nat. Neurosci. *11*, 1247–1251.

95. Wylie, L.A., Hardwick, L.J.A., Papkovskaia, T.D., Thiele, C.J., and Philpott, A. (2015). Ascl1 phospho-status regulates neuronal differentiation in a Xenopus developmental model of neuroblastoma. Dis. Model. Mech. *8*, 429–441.

96. Azzarelli, R., McNally, A., Dell'Amico, C., Onorati, M., Simons, B., and Philpott, A. (2022). ASCL1 phosphorylation and ID2 upregulation are roadblocks to glioblastoma stem cell differentiation. Sci. Rep. *12*, 2341.

97. Li, S., Mattar, P., Dixit, R., Lawn, S.O., Wilkinson, G., Kinch, C., Eisenstat, D., Kurrasch, D.M., Chan, J.A., and Schuurmans, C. (2014). RAS/ERK Signaling Controls Proneural Genetic Programs in Cortical Development and Gliomagenesis. J. Neurosci. *34*, 2169–2190.

98. Paquin, A., Hordo, C., Kaplan, D.R., and Miller, F.D. (2009). Costello syndrome H-Ras alleles regulate cortical development. Dev. Biol. *330*, 440–451.

99. Li, X., Newbern, J.M., Wu, Y., Morgan-Smith, M., Zhong, J., Charron, J., and Snider, W.D. (2012). MEK Is a Key Regulator of Gliogenesis in the Developing Brain. Neuron *75*, 1035–1050.

100. Prior, I.A., Hood, F.E., and Hartley, J.L. (2020). The Frequency of Ras Mutations in Cancer. Cancer Res. *80*, 2969–2974.

STAR★METHODS

KEY RESOURCES TABLE

REAGENT or RESOURCE	SOURCE	IDENTIFIER
Antibodies		
H-Ras Antibody (259) Alexa Fluor® 647	Santa Cruz Biotechnology	Cat# sc-35; RRID:AB_627749
rabbit anti-phospho-p44/42 MAPK (Erk1/2) (Thr202/Tyr204)	Cell Signaling Technology	Cat# 9101; RRID:AB_331646
rabbit anti-phospho-Akt (Ser473)	Cell Signaling Technology	Cat# 9271; RRID:AB_329825
mouse anti-HA.11 Epitope Tag Antibody (Clone 16B12)	BioLegend	Cat# 901501; RRID: AB_2565006
mouse anti-β-Actin (8H10D10)	Cell Signaling Technology	Cat# 3700; RRID:AB_2242334
rabbit anti-Ras (G12V Mutant Specific) (D2H12)	Cell Signaling Technology	Cat# 14412; RRID:AB_2714031
rabbit anti-Pan RAS	Cell Signaling Technology	Cat# 3965; RRID:AB_2180216
rabbit anti-p53 (D2H9O)	Cell Signaling Technology	Cat# 32532; RRID:AB_2757821
donkey anti-Rabbit IgG (H + L) Alexa Fluor™ 647	Thermo Fisher Scientific	Cat# A-31573; RRID:AB_2536183
donkey anti-Rabbit IgG (H + L) Alexa Fluor™ 488	Thermo Fisher Scientific	Cat# A-21206; RRID:AB_2535792
goat anti-Mouse IgG (H + L) Alexa Fluor™ 555	Thermo Fisher Scientific	Cat# A21422; RRID: AB_2535844
goat anti-mouse IgG H&L (HRP)	Abcam	Cat# ab205719; RRID:AB_2755049
goat anti-rabbit IgG H&L (HRP)	Abcam	Cat# ab6721; RRID:AB_955447
Chemicals, peptides, and recombinant proteins		
RepSox(TGF-β inhibitor)	Selleck Chemicals	Cat# S7223
Recombinant Human BDNF Protein	R&D Systems	Cat# 248-BDB-050
Recombinant Human CNTF Protein	R&D Systems	Cat# 257-NT-050
Recombinant Human GDNF Protein	R&D Systems	Cat# 212-GD-050
Recombinant Human Protein FGF-Basic (154 a.a.)	Peprotech	Cat# 100-18B
DMEM	Genesee Scientific	Cat# 25-500
Fetal Bovine Serum	Genesee Scientific	Cat# 25-514H
HEPES	Sigma-Aldrich	Cat# H3375
DMEM/F-12, no glutamine	Thermo Scientific	Cat# 21-331-020
B-27™ Supplement (50X), serum free	Thermo Scientific	Cat# 17-504-044
N-2 Supplement (100X)	Thermo Scientific	Cat# 17-502-048
GlutaMAX™ Supplement	Thermo Scientific	Cat# 35-050-061
DNase	Worthington Biochemical	Cat# 9003-98-9
Papain	Worthington Biochemical	Cat# 9001-73-4
Gelatin	Sigma-Aldrich	Cat# G1890
Lenti-X™ Concentrator	Takara Bio	Cat# 631232
PD0325901 (MEK inhibitor)	Sigma-Aldrich	Cat# PZ0162
MK-2206 (AKT inhibitor)	Ambeed	Cat# A145592
SP600125 (JNK inhibitor)	Ambeed	Cat# A155219
Phorbol 12-myristate 13-acetate (PMA)	Ambeed	Cat# A175370
Nuclear Fast Red Stain	StatLab	Cat# STNFR100
RIPA Buffer	Cell Signaling Technology	Cat# 9806
PMSF	Cell Signaling Technology	Cat# 8553
SNAP-Cell® TMR-Star	New England Biolabs	Cat# S9105S
Poly(ethyleneimine)	Sigma-Aldrich	Cat# P3143
Polybrene	Sigma-Aldrich	Cat# H9268
KnockOut™ DMEM	Thermo Fisher Scientific	Cat# 10-829-018
Trypsin-EDTA	Genesee Scientific	Cat# 25-510

(*Continued on next page*)

Continued

REAGENT or RESOURCE	SOURCE	IDENTIFIER
Critical commercial assays		
CellTrace™ Violet Cell Proliferation Kit, for flow cytometry	Thermo Scientific	Cat# C34557
β-Galactosidase Staining Kit	Cell Signaling Technology	Cat# 9860
Bradford Protein Assay Kit	Genesee Scientific	Cat# 18-442
Monarch® Total RNA Purification Kit	New England Biolabs	Cat# T2010S
ERCC RNA Spike-In Mix	Thermo Fisher Scientific	Cat# 4456740
NEBNext® Ultra™ II Directional RNA Library Prep Kit	New England Biolabs	Cat# E7760
4–15% Mini-PROTEAN® TGX™ precast gel	Bio-Rad	Cat# 4561086
iBlot™ 2 Transfer Stacks	Thermo Scientific	Cat# IB24001
SuperSignal™ West Femto Maximum Sensitivity Substrate	Thermo Scientific	Cat# 34096
Deposited data		
RNA seq	This study	GEO: GSE303587
Raw and analyzed data	This study	Zenodo: https://doi.org/10.5281/zenodo.16576807
Experimental models: Cell lines		
Human: HEK293T	ATCC	Cat#CRL-3216
Human: Plat-E Retroviral Packaging Cell Line	Cell Biolabs, Inc.	Cat#RV-101
Experimental models: Organisms/strains		
Mouse: C57BL/6J	The Jackson Laboratory	Cat# 000664; RRID: IMSR_JAX:000664
Mouse: B6.Cg-Tg(Hlxb9-GFP)1Tmj/J	The Jackson Laboratory	Cat# 005029; RRID: IMSR_JAX:005029
Recombinant DNA		
pMXs-NIL	Addgene	Addgene #233154
pMXs-p53DD	Addgene	Addgene #22729
pMXs-SNAP-p53DD	This study	Addgene #244168
pMXs-HRAS(G12V)	Addgene	Addgene #233181
pLentiX1-CAG-mRuby2-HRAS(G12V)	This study	Addgene #244165
pLentiX1-CAG-TagBFP	This study	Addgene #244166
pMXs-HRAS(G12V)-IRES-p53DD	Addgene	Addgene #233185
pMXs-p53DD-IRES-HRAS(G12V)	Addgene	Addgene #233187
pMXs-HRAS(G12V)-IRES-SNAP-p53DD	Addgene	Addgene #233200
pMXs-SNAP-p53DD-IRES-HRAS(G12V)	Addgene	Addgene #233198
pMXs-Isl1-T2A-mLhx3	Addgene	Addgene #233160
pMXs-mNgn2-x3HA	Addgene	Addgene #233189
pMXs-9SA.mNgn2-x3HA	This study	Addgene #244167
psPax2	Addgene	Addgene #12260
pMD2.G/VSVG	Addgene	Addgene #12259
Software and algorithms		
Adobe Illustrator CC	Adobe Systems	https://www.adobe.com
Python 3	–	https://www.python.org
FlowJo	–	https://www.flowjo.com
ImageJ	–	https://imagej.net/
GitHub	–	https://github.com/GallowayLabMIT/article-MAPK-chemogenetic-tuning; https://doi.org/10.5281/zenodo.16739843

EXPERIMENTAL MODEL AND STUDY PARTICIPANT DETAILS

Cell lines and tissue culture

Mouse embryonic fibroblasts (MEFs), Platinum-E (Plat-E), and HEK293T cells were cultured in Dulbecco's Modified Eagle Medium (DMEM) (Genesee Scientific, 25–501) supplemented with 10% fetal bovine serum (FBS) (Genesee Scientific, 25-514H) and incubated

at 37°C and 5% CO_2. Every 3 passages, Plat-Es were selected with 10 μg/mL blasticidin and 1 μg/mL puromycin. Cells were counted using a hemocytometer when seeding. All cells were routinely tested for mycoplasma contamination.

MEF dissection and isolation

Primary mouse embryonic fibroblasts (MEFs) were isolated as described in Wang et al.[31] E14.5 embryos were harvested from mice after crossing a heterozygous Hb9GFP reporter mouse with a wild type (C57BL/6) mouse. Hb9GFP-positive embryos were identified using a blue laser to detect GFP expression in the spinal cord. The head and internal organs were removed from the embryo, followed by mechanical dissociation of the remaining tissue with razor blades. The tissue was further dissociated using 0.25% trypsin-EDTA (Genesee Scientific, 25–510), first using razor blades and then via trituration. After neutralization with DMEM +10% FBS, centrifugation, and resuspension, the cells were passed through a 40 μm cell strainer to obtain a single cell suspension. Cells were plated onto 0.1% gelatin coated 10 cm dish (1 embryo per dish). At ∼80% confluency, each dish was dissociated split onto 3 gelatin coated dishes. Once the dishes reached ∼80% confluency again, the MEFs were cryopreserved in 90% FBS and 10% DMSO and stored in liquid nitrogen. MEFs were tested for mycoplasma before use. All procedures have been approved and conform with MIT Committee on Animal Care standards.

METHOD DETAILS

Plasmid construction

Plasmids were constructed using Gibson and Golden Gate cloning methods. Retroviral plasmids were cloned via LR recombination into the pMXs-WPRE-DEST plasmid. Lentiviral plasmids were cloned via LR into a pLentiX1-Harbor plasmid. All viral plasmids were confirmed using whole plasmid sequencing or Sanger sequencing.

Retroviral transduction and conversion of MEFs to iMNs

For retrovirus production, Plat-Es were seeded at 0.9 million per well onto 6-well plates coated with 0.1% gelatin for at least 5 min. The next day, Plat-Es were transfected with 1.8 μg of transfer plasmid per 6-well using a 4:1 ratio of μg PEI:μg DNA in KnockOut DMEM (ThermoFisher Scientific, 10-829-018). After 18 h, the media was replaced with 1.25 mL of 25 mM HEPES buffered DMEM +10% FBS. 24 and 48 h later, the viral supernatant was collected and filtered using 0.45 μm PES syringe filters. Culture media was replenished after the first virus collection.

Primary MEFs were thawed from cryopreserved stocks three days prior to transduction into a gelatin coated T-75 flask, and seeded at 10k cells per 96-well onto gelatin coated plates at 1 day prior to transduction. The next two days, MEFs are transduced with freshly collected and filtered virus. Each 96-well receives 11 μL of each virus for a given condition diluted in media to a final volume of 100 μL per 96-well, with a final concentration of 5 μg/mL polybrene (Sigma-Aldrich, H9268) to increase transduction efficiency. At 1 day post infection (1 dpi), virus-containing media is replaced with fresh DMEM +10% FBS.

At 3 dpi, the culture media was replaced with N3 media (DMEM/F12 (Fisher Scientific, 21331020) containing N2 (Fisher Scientific, 17-502-048), B27 (Thermo Scientific, 17504044), and 1% Glutamax (Thermo Fisher Scientific, 35050061); neurotropic growth factors – BDNF, GDNF, CNTF, and FGF (R&D Systems) – were added immediately before use to a final concentration of 10 ng/mL). Experimental conditions with $HRAS^{G12V}$ also included the small molecule RepSox (Selleck Chemicals, S7223) at 7.5 μM starting at 3 dpi. N3 media is replaced every 2 to 3 days until 14 dpi. At 14 dpi, cells were dissociated using DNase and papain. One vial each of DNase and papain (Worthington Biochemical, LK003172 and LK003178) were reconstituted in 8 mL of DMEM/F12. 40 μL of DNase/papain solution was used per 96-well and allowed to incubate at 37°C for ∼15 min or until cells detached. After dissociation, cells were resuspended in 250 μL PBS for analysis via flow cytometry. iMNs were gated on a population of bright Hb9GFP+ cells. Dim Hb9GFP+ cells were excluded from iMN quantification. iMN yield and purity were calculated as follows:

$$\text{Yield} = (\%)\ \text{iMN yield per MEF plated} = \frac{\#\ \text{iMNs at 14 dpi}}{10,000\ \text{MEFs seeded initially}} \times 100\%,$$

$$\text{Purity} = (\%)\ \text{iMN of all cells} = \frac{\#\ \text{iMNs at 14 dpi}}{\text{total}\ \#\ \text{cells at 14 dpi}} \times 100\%.$$

Lentiviral production in HEK293Ts

HEK293T cells were seeded at 6 million per 10 cm dish coated with 0.1% gelatin. The next day, each plate of 293Ts were co-transfected with 6 μg packaging plasmid (psPax2, Addgene #12260), 12 μg envelope plasmid (pMD2.G/VSVG, Addgene #12259), and 6 μg of lentivirus transfer plasmid using a 4:1 ratio of μg PEI:μg DNA. 6–8 h later, the media was replaced with 6.5 mL of 25 mM HEPES buffered DMEM +10% FBS. 24 and 48 h after the media change, viral supernatant was collected and stored at 4°C, replenishing with fresh media after the first collection. After the second collection, viral supernatant was filtered with 0.45 μm PES filters, mixed with Lenti-X concentrator (Takara Bio, 631232) at a 3:1 volume ratio of viral supernatant:Lenti-X, and then stored overnight at 4°C. The

next day, the virus mixtures were centrifuged at 1500 × g for 45 min at 4°C to pellet the virus. After removing the supernatant, the pellet was resuspended in 250 μL of media per original 10 cm plate. Concentrated virus was either kept at 4°C for less than a week, or stored at −80°C for longer periods.

Functional titer measurement and quantification

MEFs were seeded at 10k per well onto 96-well plates coated with 0.1% gelatin for at least 5 min. Two days later, cells were transduced with a serial dilution of lentivirus. The starting volume of virus was 5 μL of concentrated lentivirus per 96-well, with a 4x series dilution into 4 more wells for a total of 5 virus concentrations. Lentivirus was diluted in DMEM +10% FBS so that each well had a final volume of 100 μL per 96-well, with a final concentration of 5 μg/mL polybrene to increase transduction efficiency. After adding the virus, the cells were spinfected by centrifuging the plate at 1500 × g for 30 min at 32°C to further increase transduction efficiency. 24 h later at 1 dpi, the virus containing media was replaced with fresh DMEM +10% FBS. At 2 dpi, the cells were dissociated using trypsin, and the infection efficiency was measured via flow cytometry.

The fraction of fluorescent-positive cells was calculated for each well. To ensure single-integration events, only wells with infection rates below 40% were used for titer calculations. The functional titer in transducing units (TU) per μL was then calculated as follows:

$$Titer\left[\frac{TU}{\mu L}\right] = \frac{Numer\ of\ Cells\ Seeded * Fraction\ Positive}{Volume\ Virus\ (\mu L)}.$$

Functional titer values were used to calculate the volume of concentrated lentivirus needed for specific multiplicities of infection (MOIs). For example, seeding 10k MEFs in a 96-well required 10,000 TU for MOI 1 or 50,000 TU for MOI 5.

Lentiviral transduction of MEFs

For experiments combining lentivirus and retrovirus during conversion, lentivirus was added on the second day of retroviral infection. Mixtures containing both viruses were made so that each well received 11 μL of each retrovirus, the calculated volume of each lentivirus for the desired MOI (based on functional titer), and DMEM +10% FBS to reach a volume of 100 μL per 96-well. 5 μg/mL of polybrene was included to increase transduction efficiency. After adding the virus mixtures, the cells were spinfected by centrifuging the plate at 1500 × g for 30 min at 32°C. Conversion or twin plate protocols were then followed as described.

Twin plate conversion assay

MEFs from the same frozen batch, and therefore biological source, were seeded onto two 96-well plates. Cells were transduced with retrovirus for two days, and with lentivirus on the second day of retroviral infection, as described here. The total lentiviral MOI was 20 across both viruses. For example, in conditions with mRuby2-RAS at MOI 5, the TagBFP MOI was 15. One biological twin was dissociated with trypsin at 4 dpi and flowed to measure mRuby2-RAS expression levels. The other biological twin was dissociated with DNase/papain at 14 dpi to measure iMN yield and purity.

Conversion with signaling pathway inhibitors and PMA

The MEK inhibitor PD0325901 (Sigma-Aldrich, PZ0162), AKT inhibitor MK-2206 (Ambeed, A145592), JNK inhibitor SP600125 (Ambeed, A155219), and PMA (Ambeed, A175370) were dissolved in DMSO and stored at −20°C or −80°C. Before use, stock solutions were diluted in DMSO to reach 500x or 1000x the desired working concentration. This ensures equal DMSO concentrations across conditions. Each dilution was then added to the culture media immediately prior to use. All experiments with these small molecules began treatment at 1 dpi and continued through the experimental endpoint, with media changes every 2–3 days. For PMA experiments, RepSox was also added to all conditions beginning at 3 dpi. For immunofluorescent staining and western blot lysate, cells were treated with fresh media containing the inhibitors or PMA 20 min prior to fixation or lysis.

CellTrace proliferation assay

At 1 dpi, cells were labeled with CellTrace Violet (CTV) dye from a CellTrace proliferation kit (Thermo Scientific, C34557). First, the CTV stock solution is diluted in PBS to a final concentration of 5 μM. After washing cells with PBS, 40 μL of the CTV working solution was added per 96-well, and the plate was incubated for 30 min at 37°C. After incubation, the CTV solution was removed and replaced with fresh DMEM +10% FBS. Next cells were returned to the incubator or treated according to the experiment. At 4 dpi, cells were dissociated using trypsin and analyzed via flow cytometry. The hyperproliferative gate for each replicate was set based on the 20% of cells with lowest CTV signal in a control Puro infected condition.

Flow cytometry

All flow experiments were performed with an Attune NxT flow cytometer. Cells were gated for live and single cells from the FSC and SSC channels using FlowJo. Single cells were exported as csv files and analyzed using Python. A 405 nm laser with 440/50 filter was used for TagBFP and CTV. A 488 nm laser with a 510/10 filter was used for Hb9GFP. A 561 nm laser with a 615/25 filter was used for mRuby2 and Alexa Fluor 555.

Fixation and immunofluorescent staining

Cells were fixed with 4% paraformaldehyde for 1 h at 4°C, then washed three times with PBS. Then cells were permeabilized with 0.5% Tween 20 in PBS for 1 h at 4°C, followed by blocking in 5% FBS and 0.1% Tween 20 in PBS (blocking buffer) for 1 h at 4°C. Next, cells were incubated with primary antibodies diluted in blocking buffer overnight at 4°C. The next day, cells were wash three times with 0.1% Tween 20 in PBS and incubated with secondary antibodies diluted in blocking buffer for 1 h at 4°C. After three additional washes, nuclei were stained with 0.1 μg/mL DAPI in PBS for 30 min at room temperature. Finally, the DAPI solution was removed and cells were kept in PBS for imaging. Fluorescent images were taken using a Keyence All-in-one fluorescence microscope BZ-X800.

The primary antibodies used for immunofluorescent staining were: H-Ras Antibody (259) Alexa Fluor 647 (1:50, Santa Cruz Biotechnology, sc-35, RRID:AB_627749); Phospho-p44/42 MAPK (Erk1/2) (Thr202/Tyr204) (1:250, Cell Signaling Technology, #9101, RRID:AB_331646); Phospho-Akt (Ser473) (1:50, Cell Signaling Technology, #9271, RRID:AB_329825). The secondary antibodies used here were: Donkey anti-Rabbit IgG (H + L) Alexa Fluor 647 for ppERK (1:250k, Thermo Fisher Scientific, A-31573, RRID:AB_2536183); Donkey anti-Rabbit IgG (H + L) Alexa Fluor 488 for pAKT (1:50k, Thermo Fisher Scientific, A-21206, RRID: AB_2535792).

Immunofluorescent staining for flow cytometry

MEFs were seeded as infected as described here, except at a 24-well scale with amounts scaled up by the well surface area. MEFs were seeded at 60k per 24-well, and 66 μL of each retrovirus was used per well during the infection. At 4 days post infection, cells were dissociated using trypsin and transferred to microcentrifuge tubes. Between each staining step, cells were pelleted by centrifuged at 400 × g at 4°C, and the supernatant was removed. First, cells were fixed in 4% paraformaldehyde for 15 min at room temperature, followed by a PBS wash. Next, cells were permeabilized in 0.5% Tween 20 in PBS for 15 min at room temperature. The cells were then incubated overnight at 4°C with primary antibody diluted in blocking buffer (5% FBS and 0.1% Tween 20 in PBS). The next day, cells were washed with 0.1% Tween 20 in PBS, then incubated for 1 h at 4°C with secondary antibody diluted in blocking buffer. Finally, cells were washed again with 0.1% Tween 20 in PBS, resuspended in PBS, and then analyzed via flow cytometry.

The primary antibody used in immunofluorescent staining for flow cytometry was: anti-HA.11 Epitope Tag Antibody (Clone 16B12) (1:250, BioLegend, #901501, RRID: AB_2565006). The secondary antibody used was: Goat anti-Mouse IgG (H + L) Alexa Fluor 555 (1:250, Thermo Fisher Scientific, A21422, RRID: AB_2535844)

Senescence-associated β-galactosidase staining

β-gal staining was performed using a β-Galactosidase Staining Kit (Cell Signaling Technology, #9860) according to manufacturer's instructions. In brief, cells were washed once with PBS, fixed with Fixative Solution for 15 min at room temperature, and washed three times with PBS. Next, 50 μL of 1x β-Galactosidase Staining Solution (prepared from 10x staining solution, 100x solution A, 100x solution B, and X-gal dissolved in DMSO, adjusted to pH 6.0) was added to each well. Plates were sealed with parafilm and incubated overnight in a dry incubator at 37°C. The following day, the staining solution was removed and washed away with PBS. Next, cells were incubated with Nuclear Fast Red Stain (StatLab, STNFR100) for 10 min at room temperature, then washed three times with PBS. Brightfield images of β-gal staining were captured using a Keyence BZ-X800 microscope.

Western blot

MEFs were seeded and infected as described here, except at a 6-well scale with amounts scaled up by well surface area. MEFs were seeded at 300k per 6-well, and 330 μL of each retrovirus was used per well. Cell lysate was collected at 4 dpi. To prepare lysate, cells were first washed with ice-cold PBS, followed by the addition of 67 μL 1x RIPA buffer (Cell Signaling Technology, #9806) containing 1 mM PMSF (Cell Signaling Technology, #8553) per 6-well. Plates were incubated on ice for 5 min, then cells were detached using a cell scraper. Cells were sheared using blunt 21-gauge needles, and the lysate was clarified by centrifugation at 14000 × g at 4°C. Protein concentration was determined using a Bradford assay (Genesee Scientific, 18–442). Samples were separated using electrophoresis in a hand poured 12.5% bis-tris gel or a 4–15% Mini-PROTEAN TGX precast gel (Bio-Rad, # 4561086), with 15 μg of total cell protein loaded per well. Proteins were transferred to a PVDF membrane using the iBlot 2 Dry Blotting System. Membranes were blocked with blocking buffer (5% milk and 0.1% Tween 20 in PBS) for 1 h at room temperature with agitation. Then, membranes were incubated overnight with primary antibodies diluted in 10% blocking buffer. The next day, the membranes were washed with 0.1% Tween 20 in PBS followed by incubation with HRP-conjugated secondary antibodies in 10% blocking buffer for 1 h at room temperature. After washing. HRP signals were detected using SuperSignal West Femto Maximum Sensitivity Substrate (Thermo Scientific, 34096), and blots were imaged using the ChemiDoc MP Imaging System. Western blot band intensities were quantified using the ImageJ gel analyzer tool.

The primary antibodies used in this study were: mouse anti-β-Actin (8H10D10) (1:50k, Cell Signaling Technology, #3700, AB_2242334); rabbit anti-Ras (G12V Mutant Specific) (D2H12) (1:2k, Cell Signaling Technology, #14412, RRID:AB_2714031); rabbit anti-Pan RAS (1:20k, Cell Signaling Technology, #3965, RRID:AB_2180216); rabbit anti-phospho-p44/42 MAPK (Erk1/2) (Thr202/Tyr204) (1:30k, Cell Signaling Technology, #9101, RRID:AB_331646); rabbit anti-p53 (D2H9O) (1:20k, Cell Signaling Technology, #32532, RRID:AB_2757821), anti-HA.11 Epitope Tag Antibody (Clone 16B12) (1:10k, BioLegend, #901501, RRID: AB_2565006). The secondary antibodies used in the study were: goat anti-mouse IgG H&L (HRP) (1:50k, Abcam, ab205719, RRID: AB_2755049); goat anti-rabbit IgG H&L (HRP) (1:50k, Abcam, ab6721, RRID:AB_955447).

Bulk RNA sequencing

MEFs were seeded and infected as described here, except at a 6-well scale with amounts scaled up according to well surface area. MEFs were seeded at 300k per 6-well, and 330 μL of each retrovirus was used per well during the infection. At 4 days post infection, conditions expressing SNAP-p53DD were stained using a fluorescent SNAP substrate (New England Biolabs, #S9105S), then all conditions were dissociated with trypsin. Cells were resuspended in N3 media and kept on ice for fluorescence-activated cell sorting (FACS).

Cells were sorted on live, single-cells for conditions without SNAP, and SNAP positive for conditions with SNAP-p53DD. Sorting was performed using a Sony MA900 cell sorter. Total RNA was extracted from 50k sorted cells using the Monarch Total RNA Purification Kit (New England Biolabs, #T2010S). ERCC RNA spike-in controls (Thermo Fisher Scientific, #4456740) were added to the lysis buffer prior to RNA isolation.

Library preparation was performed by the MIT BioMicro Center using the NEBNext Ultra II Directional RNA Prep Kit. Sequencing was also conducted by the MIT BioMicro Center using an Element AVITI24 platform with 75 bp paired end reads across one flow cell lane. Raw sequencing reads were trimmed using Trim Galore and then pseudoaligned and quantified using Salmon against the GRCm39 reference transcriptome. Read counts from Salmon quantification were normalized with PyDESeq2.

QUANTIFICATION AND STATISTICAL ANALYSIS

Quantification and statistical analysis were performed using Python. All statistical tests are two-sided independent t-tests where: $p > 0.05$ is not significant (ns); and $^{*}p \leq 0.05$, $^{**}p \leq 0.01$, $^{***}p \leq 0.001$, and $^{****}p \leq 0.0001$ are significant.

Cell Reports, Volume *44*

Supplemental information

Chemogenetic tuning reveals optimal MAPK signaling for cell-fate programming

Brittany A. Lende-Dorn, Jane C. Atkinson, Yunbeen Bae, and Kate E. Galloway

Supplementary Figures

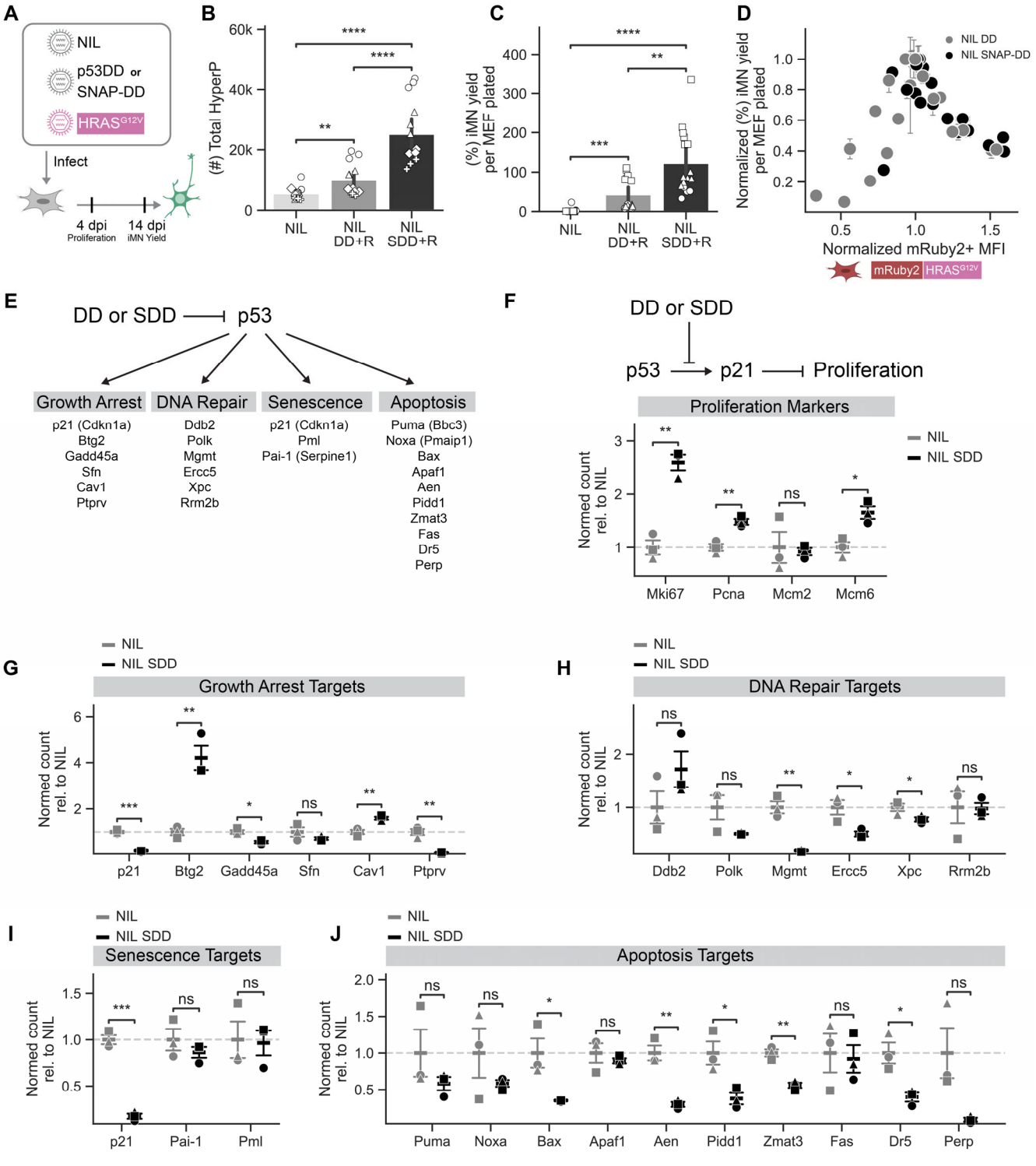

Figure S1. Comparison of p53DD and SNAP-p53DD.

A. Diagram showing experiments for comparing p53DD and SNAP-p53DD in conversion.

B-C. Total number hyperproliferative (HyperP) cells at 4 dpi and iMN yield at 14 dpi for NIL, NIL DD + $HRAS^{G12V}$ (R), or NIL SNAP-DD (SDD) + R. Mean is shown with 95% confidence interval; marker style denotes biological reps; n = 3 biological reps per condition.

D. Normalized iMN yield at 14 dpi vs. mRuby2-RAS+ geometric mean fluorescent intensity (MFI) at 4 dpi dpi for conditions with p53DD and SNAP-p53DD. Each point represents the mean of n = 3 technical replicates per bioreplicate ± standard error of mean (SEM). Marker color denotes p53DD (black) or SNAP-p53DD (grey); iMN yield is normalized so the maximum yield for each replicate overlays at 1.0 on the y-axis, and the mRuby2 levels are normalized so the mRuby2+ MFI at the MOI corresponding to the peak iMN yield overlays at 1.0 on the x-axis. n = 4 biological reps per condition.

E. Schematic of p53 functions and transcriptional targets. p53 is a transcription factor that activates genes involved in growth arrest, DNA repair, senescence, and apoptosis. p53DD and SNAP-p53DD are dominant-negative constructs that inhibit p53 activation.

F. Normalized RNA sequencing transcript counts for proliferation markers at 4 dpi in cells infected with NIL or NIL SDD. A key p53 target, p21, inhibits cell cycle progression and proliferation. SDD is expected to block p53 activation of p21, thereby promoting proliferation. Mean ± SEM is shown. Marker style denotes biological replicates (n = 3 per condition).

G-J. Normalized RNA sequencing transcript counts for p53 transcriptional target genes involved in growth arrest (G), DNA repair (H), senescence (I), and apoptosis (J). RNA was collected at 4 dpi from cells infected with NIL or NIL SDD. Mean ± SEM is shown. Marker style denotes biological reps, n = 3 biological reps per condition.

Significance summary: $p > 0.05$ (ns); $*p \leq 0.05$; $**p \leq 0.01$; $***p \leq 0.001$; and $****p \leq 0.0001$.

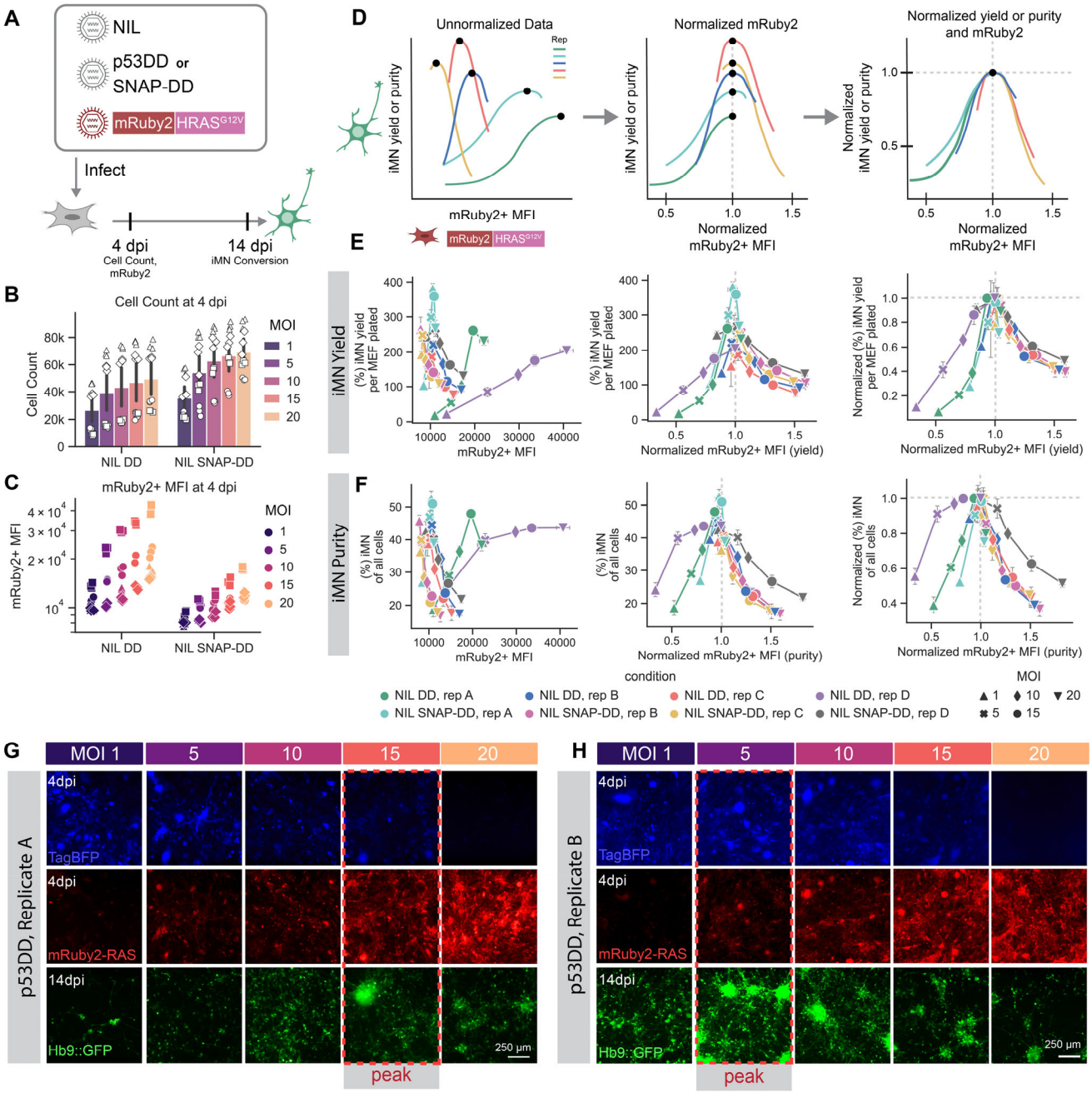

Figure S2. Cell-fate programming responds biphasically to titration of HRAS^{G12V}

A. Diagram showing experimental conditions for mRuby2-HRAS^{G12V} titration experiments.

B. Cell count at 4 dpi with mRuby2-HRAS^{G12V} MOI titration in DD and SNAP-DD conditions. Mean is shown with 95% confidence interval; marker style denotes biological replicates; n = 4 biological reps per condition.

C. mRuby2+ MFI at 4 dpi with mRuby2-HRAS^{G12V} MOI titration in DD and SNAP-DD conditions. Marker style denotes biological replicates; n = 4 biological reps per condition.

D. Schematic depicting normalization strategy to correct for variance in mRuby2+ geometric mean fluorescent intensity (MFI) and conversion efficiency across p53DD conditions and biological replicates. First, for each DD condition and replicate, mRuby2+ MFI values are normalized to the MOI value that results in the peak iMN yield or purity. Next, the yield and purity is normalized by the maximum value for each DD condition and replicate. After normalization, the peak of each condition should align at x = y = 1.0.

E-F. iMN yield (E) and purity (F) at 14 dpi vs. mRuby2-HRAS^{G12V} MFI at 4 days post infection (dpi) for conditions with p53DD and SNAP-p53DD at each stage of the normalization process. Each point represents the mean of n = 3 technical replicates ± standard error of mean (SEM). Marker style denotes MOI, hue denotes each combination of p53DD and biological replicate; n = 4 biological reps per condition.

G-H. Representative microscope images showing TagBFP and mRuby2-HRAS^{G12V} expression at 4 dpi, and corresponding Hb9::GFP expression in iMNs at 14 dpi for two separate biological replicates. The mRuby2-HRAS^{G12V} expression that correlates with peak iMN yield is indicated for each replicate. Scale bar represents 250 µm.

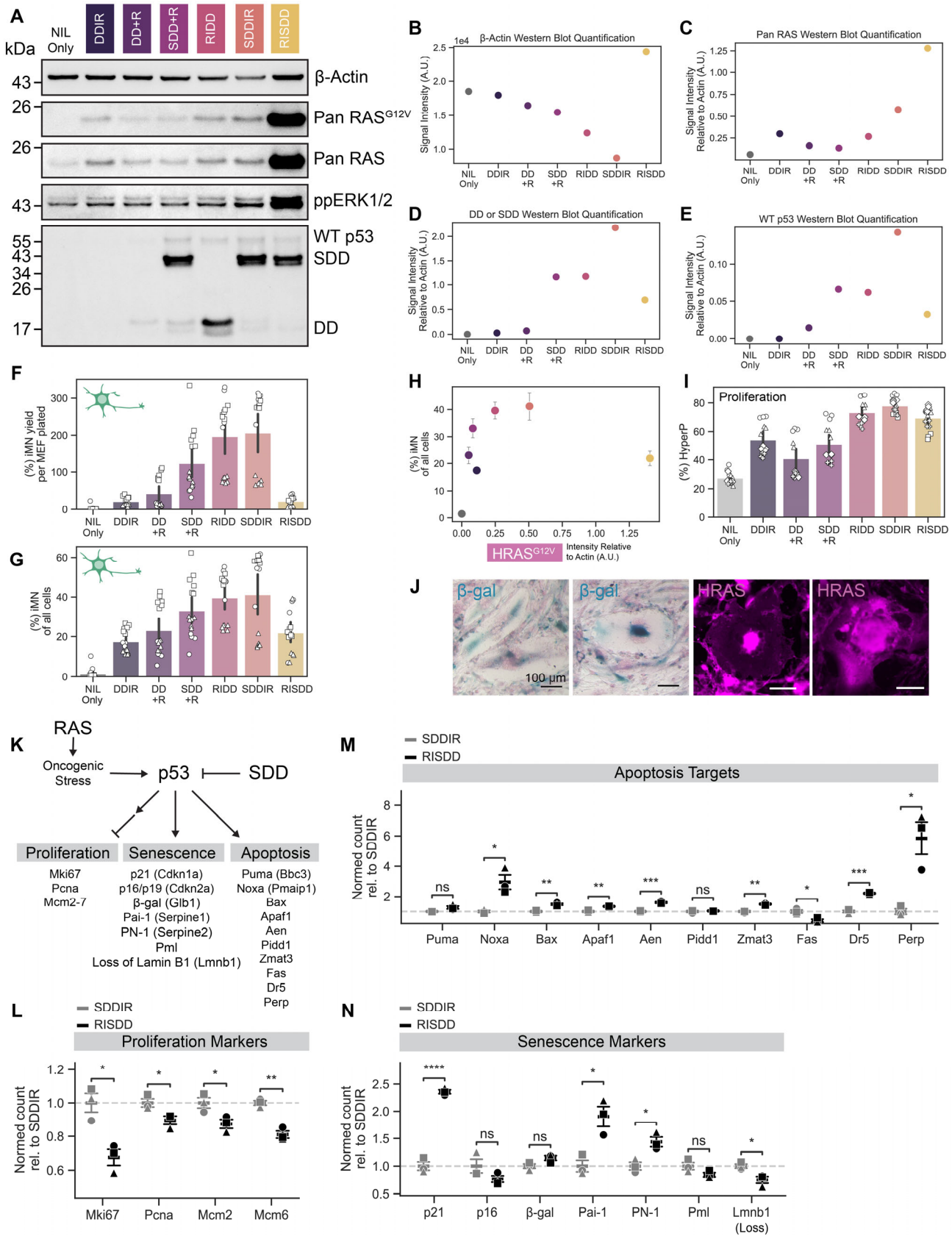
A
NIL Only
DDIR
DD+R
SDD+R
RIDD
SDDIR
RISDD
kDa
β-Actin
Pan RAS^G12V
Pan RAS
ppERK1/2
WT p53
SDD
DD
B
β-Actin Western Blot Quantification
Signal Intensity (A.U.)
C
Pan RAS Western Blot Quantification
Signal Intensity Relative to Actin (A.U.)
D
DD or SDD Western Blot Quantification
E
WT p53 Western Blot Quantification
F
(%) iMN yield per MEF plated
G
(%) iMN of all cells
H
HRAS^G12V
Intensity Relative to Actin (A.U.)
I
Proliferation
(%) HyperP
J
β-gal
HRAS
100 μm
K
RAS
Oncogenic Stress
p53
SDD
Proliferation
Senescence
Apoptosis
Mki67
Pcna
Mcm2-7
p21 (Cdkn1a)
p16/p19 (Cdkn2a)
β-gal (Glb1)
Pai-1 (Serpine1)
PN-1 (Serpine2)
Pml
Loss of Lamin B1 (Lmnb1)
Puma (Bbc3)
Noxa (Pmaip1)
Bax
Apaf1
Aen
Pidd1
Zmat3
Fas
Dr5
Perp
L
SDDIR
RISDD
Proliferation Markers
Normed count rel. to SDDIR
Mki67
Pcna
Mcm2
Mcm6
M
Apoptosis Targets
Puma
Noxa
Bax
Apaf1
Aen
Pidd1
Zmat3
Fas
Dr5
Perp
N
Senescence Markers
p21
p16
β-gal
Pai-1
PN-1
Pml
Lmnb1 (Loss)

Figure S3. HRAS^{G12V} produces biphasic conversion through MAPK signaling and proliferation.

A. Western blot of Pan RAS^{G12V}, Pan RAS, ppERK, wild type (WT) p53, SNAP-p53DD, and p53DD from lysate collected at 4 dpi with β-Actin as a loading control. All conditions include NIL. The p53 antibody recognizes all three p53 variants (WT p53, p53DD, SNAP-p53DD).

B-E. Quantification of western blots for β-Actin (B), Pan RAS (C), p53DD or SNAP-p53DD (D), and WT p53 (E) with each protein of interest normalized to β-Actin.

F-G. iMN yield and purity quantified at 14 dpi. Mean is shown with 95% confidence interval; marker style denotes biological reps; n = 3 biological reps per condition.

H. iMN purity at 14 dpi vs. Pan RAS^{G12V} expression normalized to β-Actin levels measured from a western blot. Mean iMN purity is shown ± standard error of mean (SEM).

I. Percent HyperP at 4 dpi across conditions. Mean is shown with 95% confidence interval; marker style denotes biological reps; n = 4 biological reps per condition.

J. Microscope images showing examples of senescence morphology in NIL RISDD cells stained for senescence-associated β-galactosidase (β-gal) and nuclear fast red at 2 dpi and HRAS at 4 dpi. Scale bar represents 100 μm.

K. Schematic of p53 functions and transcriptional targets. P53 is a transcription factor that activates genes involved in cellular processes such as growth arrest, DNA repair, senescence, and apoptosis. Oncogenic stress induced by mutant RAS can activate p53. p53DD and SNAP-p53DD are dominant-negative constructs that inhibit p53 activation.

L. Normalized RNA sequencing transcript counts for proliferation markers at 4 dpi in cells infected with NIL SDDIR or NIL RISDD. Marker style denotes biological reps, n = 3 biological reps per condition; t-test independent samples.

M. Normalized RNA sequencing transcript counts for p53 transcriptional targets involved in apoptosis. RNA was collected at 4 dpi from cells infected with NIL SDDIR or NIL RISDD. Mean ± SEM is shown. Marker style denotes biological reps, n = 3 biological reps per condition; t-test independent samples.

N. Normalized RNA sequencing transcript counts for genes associated with the senescence program, which may be upregulated or downregulated in senescent cells. RNA was collected at 4 dpi from cells infected with NIL SDDIR or NIL RISDD. Mean ± SEM is shown. Marker style denotes biological reps, n = 3 biological reps per condition; t-test independent samples.
Significance summary: $p > 0.05$ (ns); *$p \leq 0.05$; **$p \leq 0.01$; ***$p \leq 0.001$; and ****$p \leq 0.0001$.

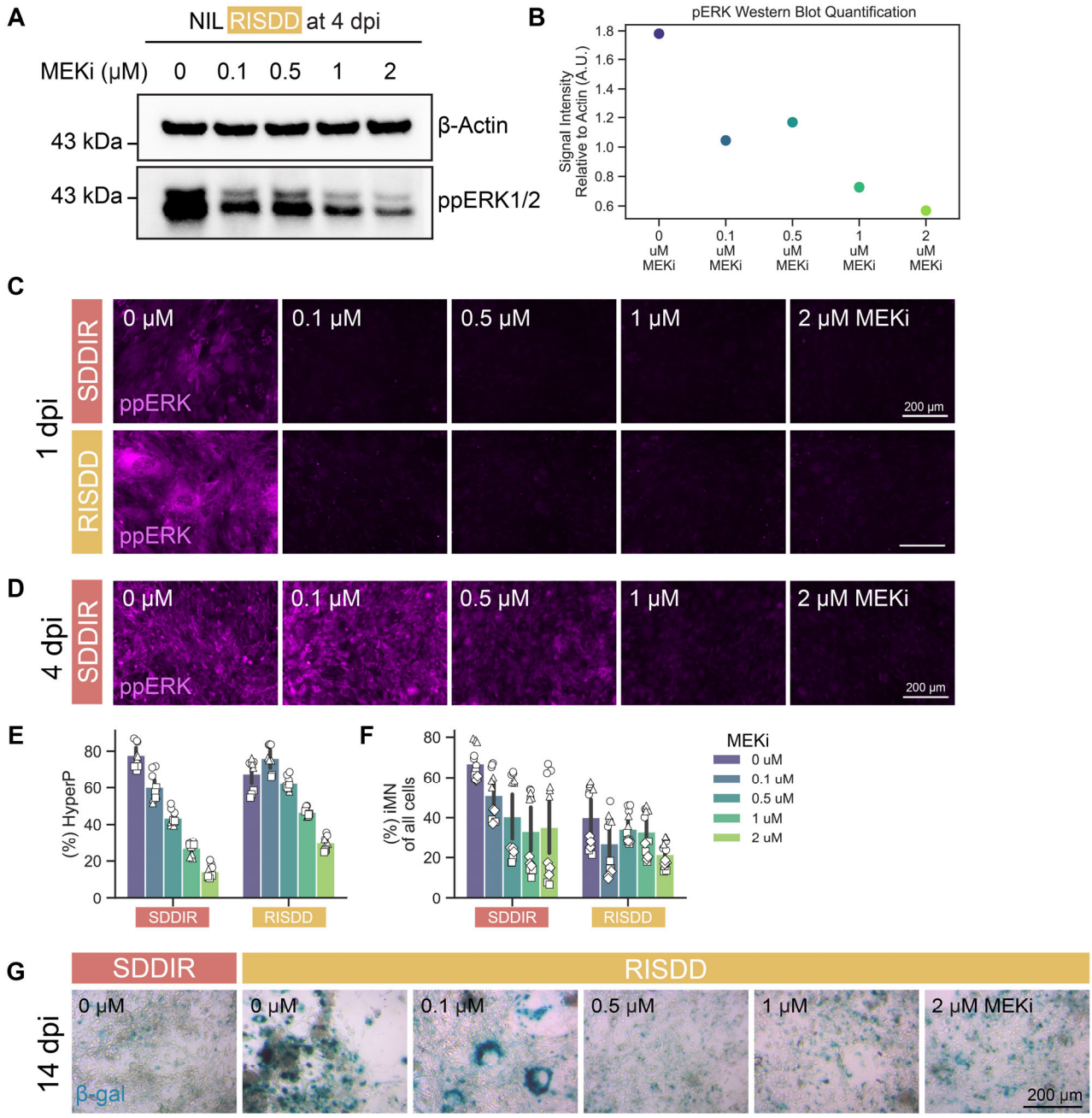

Figure S4. Tuning MAPK signaling attenuates senescence and increases conversion.

A. Western blot of ppERK from lysate collected at 4 dpi for NIL RISDD 20 minutes after treatment with fresh MEK inhibitor (PD0325901), including β-Actin as a loading control. MEKi was added to the media beginning at 1 dpi.

B. Quantification of western blot for ppERK normalized to β-Actin.

C-D. Representative images of immunofluorescent staining for ppERK at 1 and 4 dpi in the two polycistronic cassette conditions with the highest HRAS^{G12V} expression (SDDIR and RISDD) with MEKi titration. MEKi was added to the media beginning at 1 dpi. Scale bar represents 200 μm.

E-F. Percent HyperP at 4 dpi and iMN purity at 14 dpi for with a MEK inhibitor titration for the two polycistronic cassettes with highest HRAS^{G12V} expression. Mean is shown with 95% confidence interval; marker style denotes biological reps; n =3 biological reps per condition.

G. Representative images of cells stained for senescence-associated β-galactosidase (β-gal) at 14 dpi with MEKi titration. MEKi was added to the media beginning at 1 dpi. Scale bar represents 200 μm.

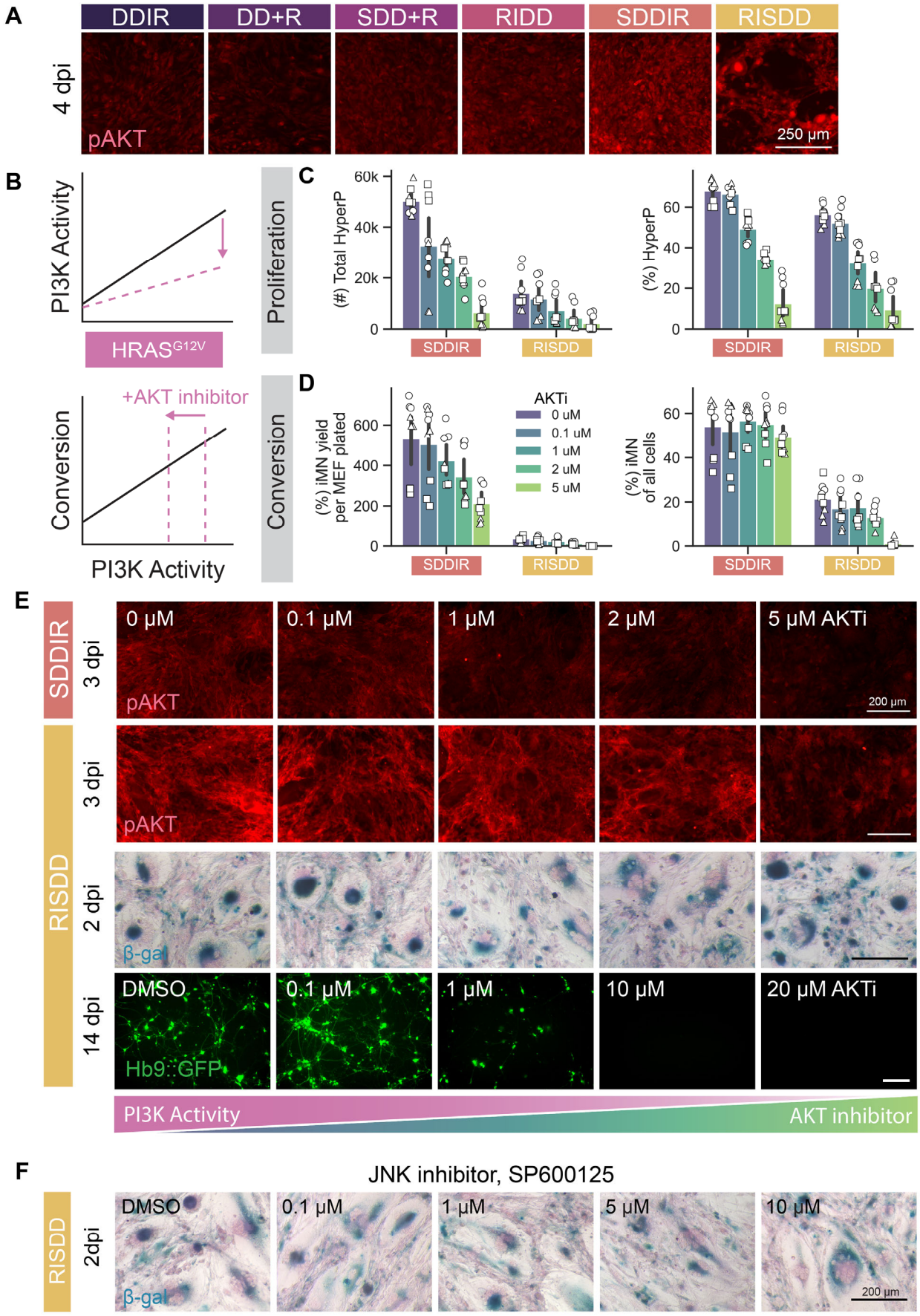
A
DDIR
DD+R
SDD+R
RIDD
SDDIR
RISDD
4 dpi
pAKT
250 μm
B
PI3K Activity
HRAS^{G12V}
Proliferation
C
(#) Total HyperP
60k
40k
20k
0
SDDIR
RISDD
(%) HyperP
60
40
20
0
SDDIR
RISDD
Conversion
+AKT inhibitor
PI3K Activity
Conversion
D
(%) iMN yield per MEF plated
600
400
200
0
AKTi
0 uM
0.1 uM
1 uM
2 uM
5 uM
SDDIR
RISDD
(%) iMN of all cells
60
40
20
0
SDDIR
RISDD
E
SDDIR
3 dpi
pAKT
0 μM
0.1 μM
1 μM
2 μM
5 μM AKTi
200 μm
RISDD
3 dpi
pAKT
2 dpi
β-gal
14 dpi
Hb9::GFP
DMSO
0.1 μM
1 μM
10 μM
20 μM AKTi
PI3K Activity
AKT inhibitor
F
JNK inhibitor, SP600125
RISDD
2dpi
β-gal
DMSO
0.1 μM
1 μM
5 μM
10 μM
200 μm

Figure S5. Tuning of PI3K signaling does not attenuate senescence or increase the rate of conversion.

A. Representative images of immunofluorescent staining for pAKT at 4 dpi across DD HRAS^{G12V} polycistronic cassette conditions. Scale bar represents 250 μm.
B. Diagram depicting expected results of adding an AKT inhibitor on PI3K signaling levels and conversion.
C. Total number HyperP and percent HyperP at 4 dpi with an AKT inhibitor (MK-2206) titration for the two polycistronic cassettes with highest HRAS^{G12V} expression (SDDIR and RISDD). AKTi was added to the media beginning at 1 dpi. Mean is shown with 95% confidence interval; marker style denotes biological reps; n = 3 biological reps per condition.
D. Conversion yield and purity quantified at 14 dpi with an AKT inhibitor titration for the two polycistronic cassettes with highest HRAS^{G12V} expression. AKTi was added to the media beginning at 1 dpi. Mean is shown with 95% confidence interval; marker style denotes biological reps; n = 3 biological reps per condition.
E. Representative images of cells stained for pAKT at 3 dpi in SDDIR and RISDD polycistronic cassettes, and senescence-associated β-galactosidase (β-gal) and nuclear fast red at 2 dpi and Hb9::GFP expression in iMNs at 14 dpi for the polycistronic cassette with the highest HRAS^{G12V} expression (RISDD) with AKTi titration. Scale bar represents 200 μm.
F. Representative images of cells stained for senescence associated β-gal and nuclear fast red at 2 dpi in RISDD condition after treatment with JNK inhibitor (SP600125) beginning at 1 dpi. Scale bar represents 200 μm.

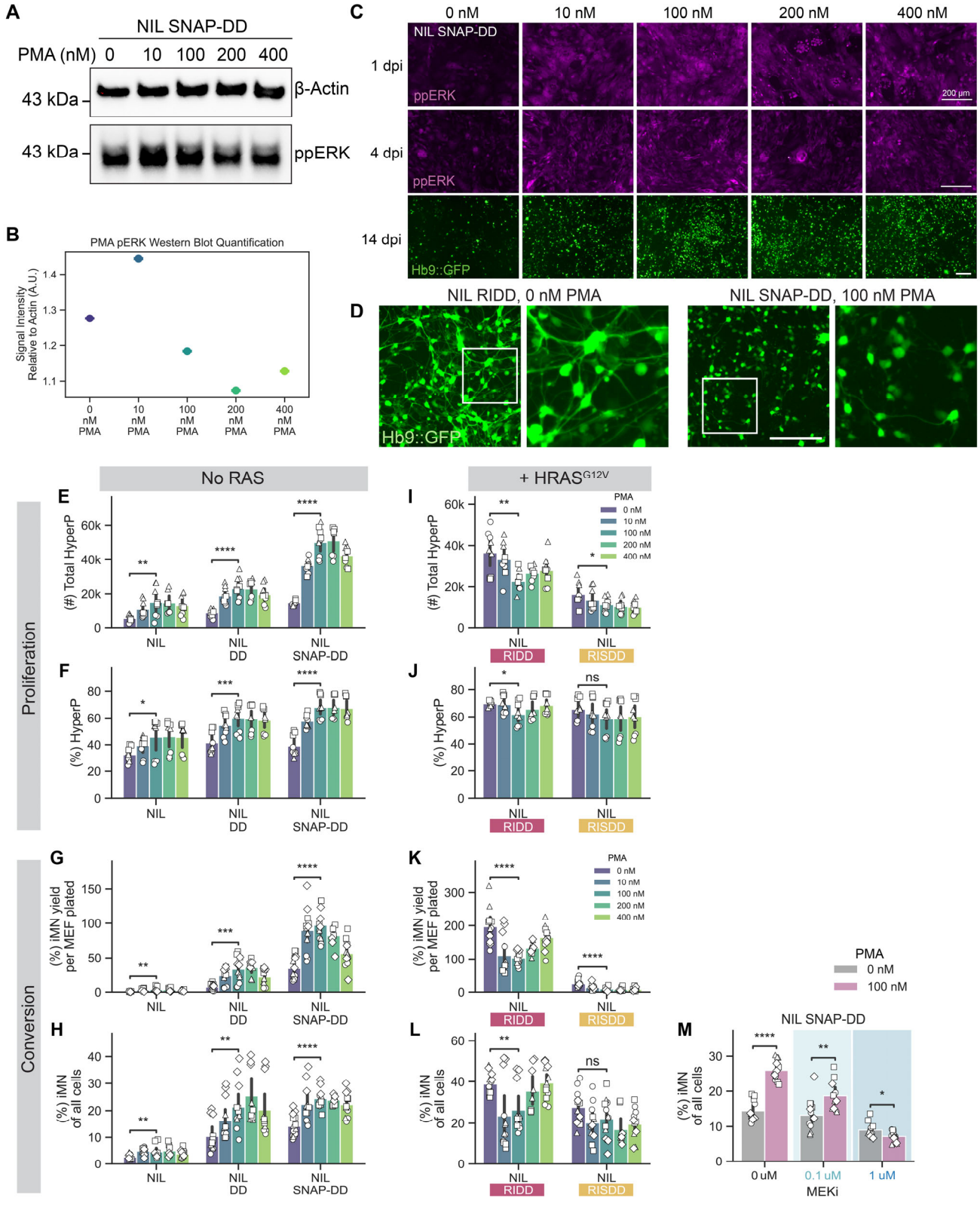
A
NIL SNAP-DD
PMA (nM) 0 10 100 200 400
43 kDa
β-Actin
43 kDa
ppERK
B
PMA pERK Western Blot Quantification
Signal Intensity Relative to Actin (A.U.)
0 nM PMA
10 nM PMA
100 nM PMA
200 nM PMA
400 nM PMA
C
0 nM
10 nM
100 nM
200 nM
400 nM
NIL SNAP-DD
1 dpi
ppERK
4 dpi
ppERK
14 dpi
Hb9::GFP
200 µm
D
NIL RIDD, 0 nM PMA
NIL SNAP-DD, 100 nM PMA
Hb9::GFP
No RAS
+ HRASG12V
Proliferation
Conversion
E
(#) Total HyperP
NIL
NIL DD
NIL SNAP-DD
F
(%) HyperP
I
NIL RIDD
NIL RISDD
PMA
0 nM
10 nM
100 nM
200 nM
400 nM
J
ns
G
(%) iMN yield per MEF plated
H
(%) iMN of all cells
K
L
M
NIL SNAP-DD
0 uM
0.1 uM
1 uM
MEKi
PMA
0 nM
100 nM

Figure S6. Activation of MAPK signaling induces high rates of conversion in the absence of mutant RAS.

A. Western blot of ppERK from lysate collected at 4 dpi for NIL SNAP-p53DD 20 minutes after a media change with fresh PMA including β-Actin as a loading control.

B. Quantification of western blot for ppERK normalized to β-Actin.

C. Representative images of immunofluorescent staining for ppERK in NIL SNAP-DD infected cells at 1 dpi or 4dpi that were fixed 20 minutes after replacing media with fresh PMA at varying concentrations, and Hb9::GFP+ iMNs at 14 dpi. Scale bar represents 200 µm.

D. Representative images comparing iMN morphology at 14 dpi for NIL RIDD without PMA to NIL SNAP-DD + 100 nM PMA. Scale bar represents 200 µm.

E-H. Total number and percent HyperP cells at 4 dpi with a PMA titration for conditions with and without $HRAS^{G12V}$. Mean is shown with 95% confidence interval; marker style denotes biological reps; n = 3 biological reps per condition; t-test independent samples.

I-L. Conversion yield and purity at 14 dpi with a PMA titration for conditions with and without $HRAS^{G12V}$. Mean is shown with 95% confidence interval; marker style denotes biological reps; n = 4 biological reps per condition; t-test independent samples.

M. Conversion purity quantified at 14 dpi for cells infected with NIL SNAP-DD and treated with combinations of 0 nM or 100 nM PMA to activate MAPK signaling and 0 µM, 0.1 µM, or 1 µM of MEK inhibitor (PD0325901) to inhibit MAPK signaling. Small molecules were added to the media beginning at 1 dpi. Mean is shown with 95% confidence interval; marker style denotes biological reps; n = 4 biological reps per condition; t-test independent samples.

Significance summary: $p > 0.05$ (ns); $*p \leq 0.05$; $**p \leq 0.01$; $***p \leq 0.001$; and $****p \leq 0.0001$.

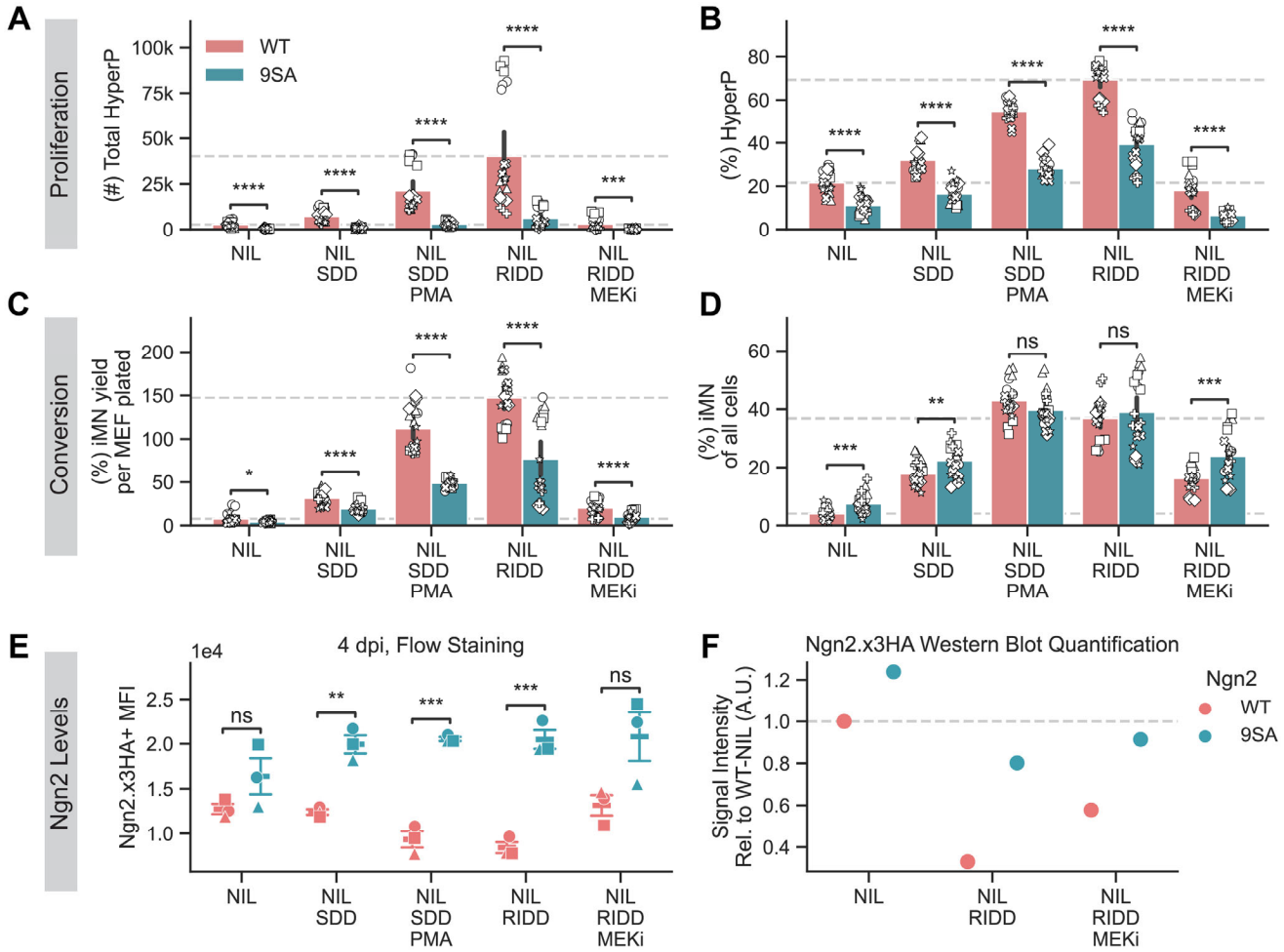

Figure S7. MAPK signaling regulates Ngn2 levels to support proliferation-dependent iMN conversion.

A-B. Total number (A) and percent (B) HyperP cells at 4 dpi for cells infected with either wild type (WT) or phospho-mutant (9SA) Ngn2 along with Isl1, Lhx3. Reprogramming conditions also include SNAP-p53DD (SDD) ± PMA and HRAS^{G12V}-IRES-p53DD (RIDD) ± MEK inhibitor (MEKi). Mean is shown with 95% confidence interval; marker style denotes biological reps; n = 6 biological reps per condition; t-test independent samples.

C-D. Conversion yield (C) and purity (D) at 14 dpi. Mean is shown with 95% confidence interval; marker style denotes biological reps; n = 6 biological reps per condition; t-test independent samples.

E. Ngn2 mean fluorescent intensity (MFI) measured via immunofluorescent flow cytometry. Mean ± SEM is shown. Marker style denotes biological reps, n = 3 biological reps per condition; t-test independent samples.

F. Ngn2 levels at 4 dpi quantified from western blot and normalized to β-Actin, shown relative to WT NIL condition.

Significance summary: $p > 0.05$ (ns); *$p \leq 0.05$; **$p \leq 0.01$; ***$p \leq 0.001$; and ****$p \leq 0.0001$.